High-resolution geodetic strain rate field reveals dynamics of the India-Eurasia collision

Authors: T.J. Wright[1]*, G.A. Houseman[1], J. Fang[1], Y. Maghsoudi[1], A.J. Hooper[1], J.R. Elliott[1], L. Evans[2], M. Lazecky[1], Q. Ou[1], B.E. Parsons[3], J.C. Rollins[1,4], L. Shen[1], H. Wang[5]

Affiliations:

[1]COMET, School of Earth and Environment, University of Leeds; Leeds, UK
[2]School of Earth, Atmosphere & Environment, Monash University, Clayton, VIC, Australia
[3]COMET, Department of Earth Sciences, University of Oxford; Oxford, UK
[4] GNS Science, Lower Hutt, New Zealand
[5] Department of Surveying Engineering, Guangdong University of Technology, Guangzhou, China

*Corresponding author. Email: t.j.wright@leeds.ac.uk

High-resolution geodetic strain rate field reveals dynamics of the India-Eurasia collision

Authors: T.J. Wright[1]*, G.A. Houseman[1], J. Fang[1], Y. Maghsoudi[1], A.J. Hooper[1], J.R. Elliott[1], L. Evans[2], M. Lazecky[1], Q. Ou[1], B.E. Parsons[3], J.C. Rollins[1,4], L. Shen[1], H. Wang[5]

Affiliations:

[1]COMET, School of Earth and Environment, University of Leeds; Leeds, UK
[2]School of Earth, Atmosphere & Environment, Monash University, Clayton, VIC, Australia
[3]COMET, Department of Earth Sciences, University of Oxford; Oxford, UK
[4] GNS Science, Lower Hutt, New Zealand
[5] Department of Surveying Engineering, Guangdong University of Technology, Guangzhou, China

*Corresponding author. Email: t.j.wright@leeds.ac.uk

Abstract: Determining the distribution of seismic hazard in the continents requires an understanding of how much deformation is accommodated by major faults. Quantifying the role of major faults in continental deformation has been hampered by a lack of high-resolution observations in the deforming interiors of continents. By combining surface movement data derived from 22,000 satellite radar images with data from sparse, ground-based GNSS stations we produce the first high-resolution present-day surface velocity field for the Tibetan Plateau and surrounding region, where the collision of rigid Indian lithosphere with Eurasia has created Earth's largest and highest deforming region. We show that continental deformation is best characterized by a combination of continuous distributed deformation and focused strain on a few major fault systems.

One-Sentence Summary: Role of major fault systems in continental deformation revealed in first high-resolution deformation map of Tibetan Plateau.

Main Text:.

Plate tectonic theory describes the motions of Earth's surface as the rotation and translation of large, rigid plates, with deformation and seismic hazard occurring in narrow zones around their boundaries (*1*). Although successful in characterizing the behavior of oceanic lithosphere (e.g. *2*) it has long been recognized that the simple kinematic rules of plate tectonics require significant adjustment to explain the wide deforming belts observed in the continents (*3*). Two end-member classes of theory have been used to explain deformation in the continents. In the first, the continents are divided into individual, smaller fault-bounded blocks, which can rotate and translate independently, acting as microplates (e.g. *4, 5*). The alternative approach has been, broadly speaking, to model the continents as a viscous fluid that deforms in response to boundary and internal forces with minimal impact from crustal faulting (e.g. *6*). Neither model can fully explain all observations, but the degree to which continental deformation is focused on major fault systems or is broadly distributed remains a contentious and open question, the solution to which has been hampered by the lack of sufficiently high-resolution observations of active deformation (*7*). Resolving this issue is also important for seismic hazard assessment as it governs the degree to which earthquakes are focused on major, mapped, "block-bounding" faults (*8*).

The Tibetan plateau is the largest deforming region in the continents and has long been the testing ground for these competing theories of continental tectonics (e.g. *9, 10*). As observations of active deformation, particularly from Global Navigation Satellite Systems (GNSS), have improved (e.g. *11, 12*), models have been refined. The number of blocks in microplate models has increased from a handful of large blocks (*4*) to more than 250 in recent models (*13*); continuum models have increased in complexity from 2D thin viscous sheet models with uniform properties (*9*), to models that incorporate variability in lithospheric rheology both laterally and with depth (*14, 15*). While it is clear that much of the present-day deformation in this region is broadly distributed, concentrations of strain accumulation have also been observed around some major faults (e.g. *16*). Quantifying the specific role of all the major fault systems in the region is now possible with continental-scale measurements of surface displacement rates obtained using satellite geodetic methods.

With more than 7 years of observations from the Sentinel-1 radar constellation (*17*), and as a result of advances in automatic InSAR processing (*18, 19*), we can reveal a near-complete map of the present-day displacement rates at the surface of the Tibetan plateau with the level of detail required to test such models. The distribution of surface deformation is consistent broadly with continuous ductile deformation that is interrupted by localized displacements on a few major fault systems. We show that these key features can be reproduced by adapting viscous continuum models to allow for focused strain on these fault systems.

To map 3D surface velocities at high resolution, we first produce a network of short-baseline Sentinel-1 interferograms in 82 ascending and 84 descending frames covering the Tibetan plateau using the COMET-LiCSAR system (*18*), spanning late 2014 to mid 2021. We use the LiCSBAS algorithm (*19*) to compute average line-of-sight surface velocities for each frame. To avoid contamination, we remove signals from coseismic deformation for earthquakes larger than M_w 5.5 before calculating the average velocities (Supplementary Methods). The line-of-sight velocities for each frame are initially independently referenced; in a second step we use a compilation of GNSS velocities in a Eurasian reference frame to carry out a joint inversion for reference frame adjustment parameters and continuous, smooth 3D velocities on a ~0.2 degree (~20 km) triangular mesh (Fig. S1, S2), regularized by Laplacian smoothing, following (*20*) (see

Supplementary Methods). The inverted reference frame parameters allow us to derive mosaics of ascending and descending line-of-sight velocities tied to the Eurasian reference frame (Fig. S3). Following (*21*), we use the Eurasian line-of-sight mosaics to solve for east-west and vertical velocities at 1 km resolution without the requirement for smoothing in areas where both ascending and descending data exist (Fig. 1, S4), using the north-south velocities from the smooth 3D velocity model as a constraint. The horizontal gradients of the continuous, smooth 3D model velocity field are used to derive horizontal strain rates in a spherical coordinate system (Fig. 2, S5) (following *22*). More details of our approach are given in the Supplementary Methods section and uncertainty maps are shown in Fig. S6.

The vertical velocity field (Fig. S4) is dominated by non-tectonic processes including deformation from permafrost, hydrology, and anthropogenic activity (*23*), as well as potentially contaminated by phase biases (*24*). However, the horizontal velocity and strain-rate fields (Figs. 1, 2) are dominated by tectonics, and reveal how the Tibetan Plateau is deforming in response to the northward motion of the Indian plate. The broad-scale deformation pattern is consistent with previous studies (e.g. *16, 25*) that show the plateau is shortening in a direction parallel to the plate-motion convergence vector of India relative to Eurasia and extending perpendicular to this direction (Fig 1). South of the Kunlun Fault, extension outpaces convergence, resulting in dilatation (Fig 2). The inclusion of InSAR data in our new velocity field sharpens the spatial resolution of deformation observations, particularly in the interior of the plateau (Fig S7). The strain-rate field clearly demonstrates that the highest strain rates in the plateau interior are focused around major, mapped strike-slip fault zones, including the Altyn Tagh, Kunlun, Haiyuan, and Xian Shui He Faults. These faults separate regions of relatively low strain rate; however, the second invariant of the strain rate tensor in the west/central Tibetan Plateau is still relatively high, with a median value of 18.2 nanostrain/year, compared to 7.0 nanostrain/year in the aseismic Tarim basin (regions shown in Fig 2). Velocity profiles that avoid crossing major faults do not in general show significant strain concentrations associated with mapped structures (Fig 1).

One striking observation in our velocity field is the high strain rates in areas that were impacted by major earthquakes in the 20-year period before the Sentinel-1 observations. This includes the 1997 Mw 7.4 Manyi earthquake, the 2001 Mw 7.8 Kokoxili earthquake, and the 2008 Mw 7.2 Yutian earthquake (Fig. 1, 2). We have not attempted to correct the InSAR data for the postseismic signal from these earthquakes. These high postseismic strain rates are consistent with studies that show elevated strain rates for decades following earthquakes (e.g. *26, 27*). For example, Hussain et al (*28*) show that strain rates on the North Anatolian Fault decay back to a steady state "interseismic" rate after around 20 years, after which focused strain around the fault is maintained for the entire inter-event period. The major strike-slip faults in the Tibetan plateau, such as the Altyn Tagh Fault, also have elevated strain rates, compared to the regions around them, even if they have not had recent earthquakes. These observations are consistent with strain rates decaying to a steady-state "interseismic" strain rate after a postseismic transient lasting decades. Focused strain rates late in the earthquake cycle require a background substrate with a relaxation time equal to or greater than the inter-event period (*28-30*).

Previous attempts to explain the deformation of Tibet using continuum models of a thin viscous layer have addressed the broad pattern of the displacement field observed by assuming a rigid India indenting Asia, with crustal thickness variations affecting gravitational potential energy, and a deformation rate governed by a non-Newtonian viscosity law (*31, 32*). But they have not been very successful at accommodating focused strain around major faults. We here use an

adapted Thin Viscous Shell model that allows localized fault displacement on pre-defined discontinuities (model faults). The calculations described here use a thin spherical shell with the gravitational potential energy calculated assuming local isostatic balance of topography from ETOPO1 (*33*), smoothed with a 20-km-width Gaussian filter . Experiments and model developments are described in full in (*34*).

In typical continental crust, faults in the seismogenic layer (shallower than about 20 km for this region) might be well represented as discontinuities in a continuum field. At deeper levels faults are thought to evolve into ductile shear zones that broaden with depth and may be tens of kilometers wide (*35, 36*). In our simplified depth-averaged model, we represent a major fault as a discontinuity in which the horizontal shear stress is proportional to the slip-rate across the fault. The proportionality constant (fault resistance coefficient f) is adjustable and can be interpreted in terms of the width and viscosity of a lithospheric-scale ductile shear zone. Thus we can examine, in the context of this deforming region, the effect of allowing slip on the modelled fault systems.

In attempting to obtain a reasonable representation of the strain-rate field in the confines of this model, we assume firstly that the lithosphere generally deforms according to a non-linear constitutive law,

$$\tau_{ij} = B\dot{E}^{(1-n)/n}\dot{\varepsilon}_{ij}$$

in which strain-rate, $\dot{\varepsilon}$, is independent of depth and varies as the nth power of depth-averaged deviatoric stress τ (*37*) with $\dot{E}$ representing the second invariant of the strain rate tensor. The viscosity coefficient B in this constitutive law is set to a constant value of 1 except in those regions representing India, and the Tarim, Sichuan and Alashan-Ordos basins, where we arbitrarily set a large value (10 times higher than background) so that they behave like nearly rigid blocks set within the deforming medium (Fig. S8). We also allow that the Tibetan plateau and Tien Shan regions are weaker by setting a smaller value there (40% of background), with south-central Tibet required to be even weaker (10% of background; Fig. S8). Apart from n, which we fix at 3, the other significant physical constant in this problem is the Argand number Ar, which sets the magnitude of the buoyancy forces relative to the internal viscous stress. We estimate this by minimizing the misfit between observed and predicted velocities. We apply boundary conditions on the external edges of the domain to simulate the relative plate rotations of India with respect to Eurasia, using the rotation pole from (*38*), and the Yangtze and Amur plates, using poles from (*2*) (Fig. S8). We evaluate a given model calculation by comparing the predicted horizontal velocities with those observed by geodesy (Fig 3).

For the purpose of comparing the geodetic velocity field and that derived from the thin viscous shell model we included a simplified representation of the following major faults: Kunlun, Haiyuan, Altyn Tagh, Sagaing, Xian Shui He and Himalyan Thrust Faults and we experimented with a range of fault resistance coefficients f (*34*). The key innovation of this type of model is the ability to more accurately represent variations in the velocity field as measured geodetically near major faults and also to test the influence of faults on the broader deformation field. The dominantly east-west oriented fault systems like the Kunlun Fault allow east-directed velocities south of the fault that are significantly increased relative to the case of continuous deformation when f is small (Fig. 1, 3). The area affected by faulting in the model is controlled by the length of the active fault; faults have a widespread influence beyond the enhanced strain zone along the fault. In the model, buoyancy-driven flow around the eastern Himalayan syntaxis, facilitated in the north by movement on the Kunlun Fault, causes widespread dilatation in South and Central

Tibet. In north-east Tibet, the model predicts contraction, supporting arguments that active topographic growth in Tibet is focused in the northeast (*39*).

We have mapped the deformation of the Tibetan plateau at high resolution for the first time. Our results highlight the importance of major faults and have important implications for the dynamics of continental tectonics. We show that major fault zones exert an influence on the broad-scale deformation field that goes beyond a localized passive response. We can explain the overall pattern of deformation and seismicity with a relatively simple model where deformation is driven by external tectonic forces and internal buoyancy forces, which interact with a ductile lithosphere comprising regions of different strength and cut by lithospheric-scale fault systems. Where the lithosphere is weak, significant strain occurs both on major faults and in the regions between. Our models can provide a physical basis for determining the distribution of seismicity in seismic hazard models.

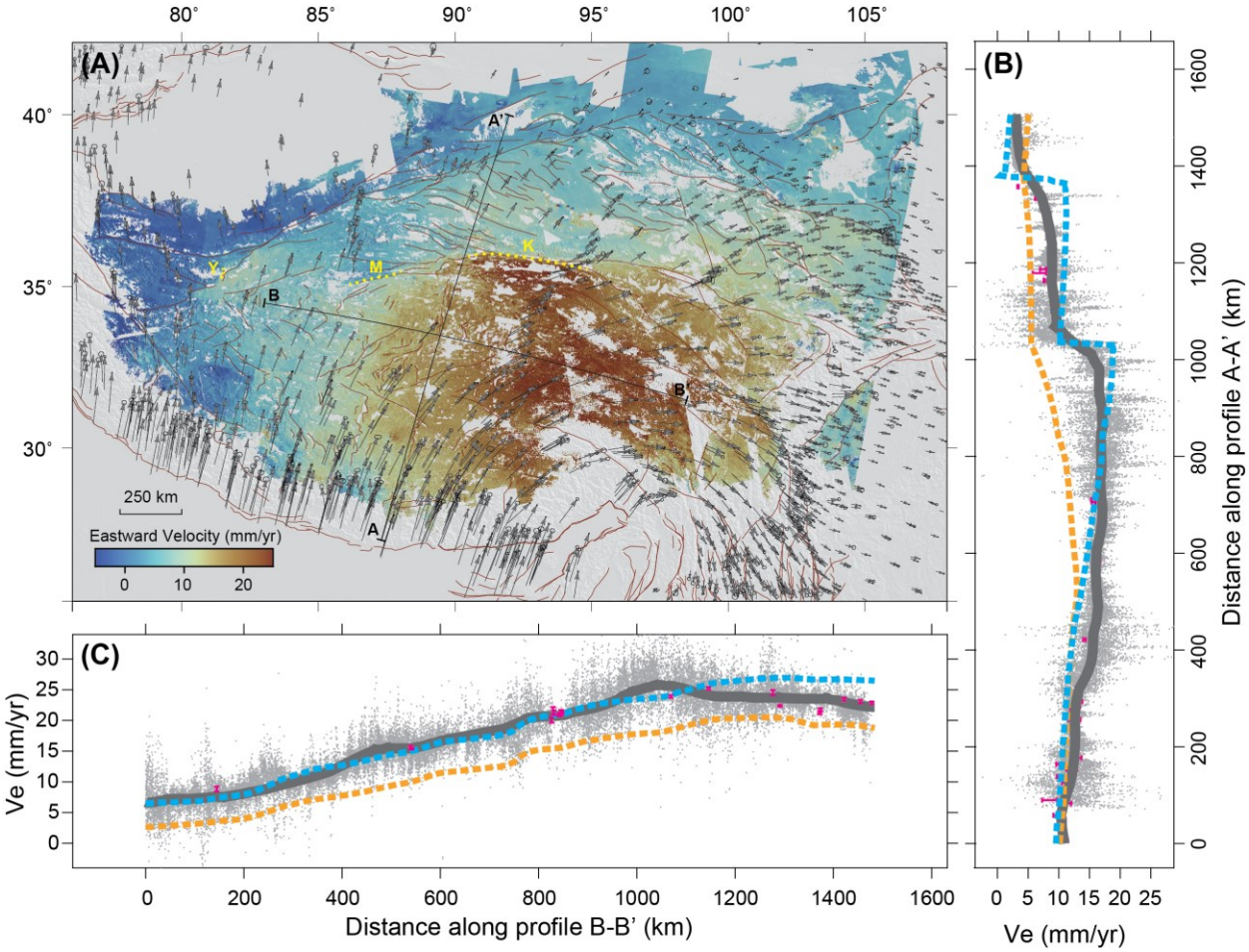

Fig. 1. High-resolution velocity field of Tibet. (a) East component of the velocity field for Tibet derived from the geo-referenced InSAR, overlain with velocity vectors obtained from GNSS (Supplementary Methods), relative to a fixed Eurasia reference frame. Faults, shown as dark red lines, are from the Global Earthquake Model (*40*), with yellow dashed lines indicating the ruptures of the 1997 Manyi (M), 2001 Kokoxili (K), and 2007 Yutian (Y) earthquakes, respectively. (b), (c) profiles of the eastward field along black lines marked A-A' and B-B' in (a). Grey dots are values from the InSAR grid within 15 km of the profile line; the grey line is the eastward component of the velocity field derived from joint inversion of InSAR and GNSS; magenta bars show GNSS east velocities and their uncertainties within 75 km of the profile; the cyan dashed line is the prediction of our best-fit geodynamic model; the orange dashed line is the best geodynamic model we could obtain without including faults.

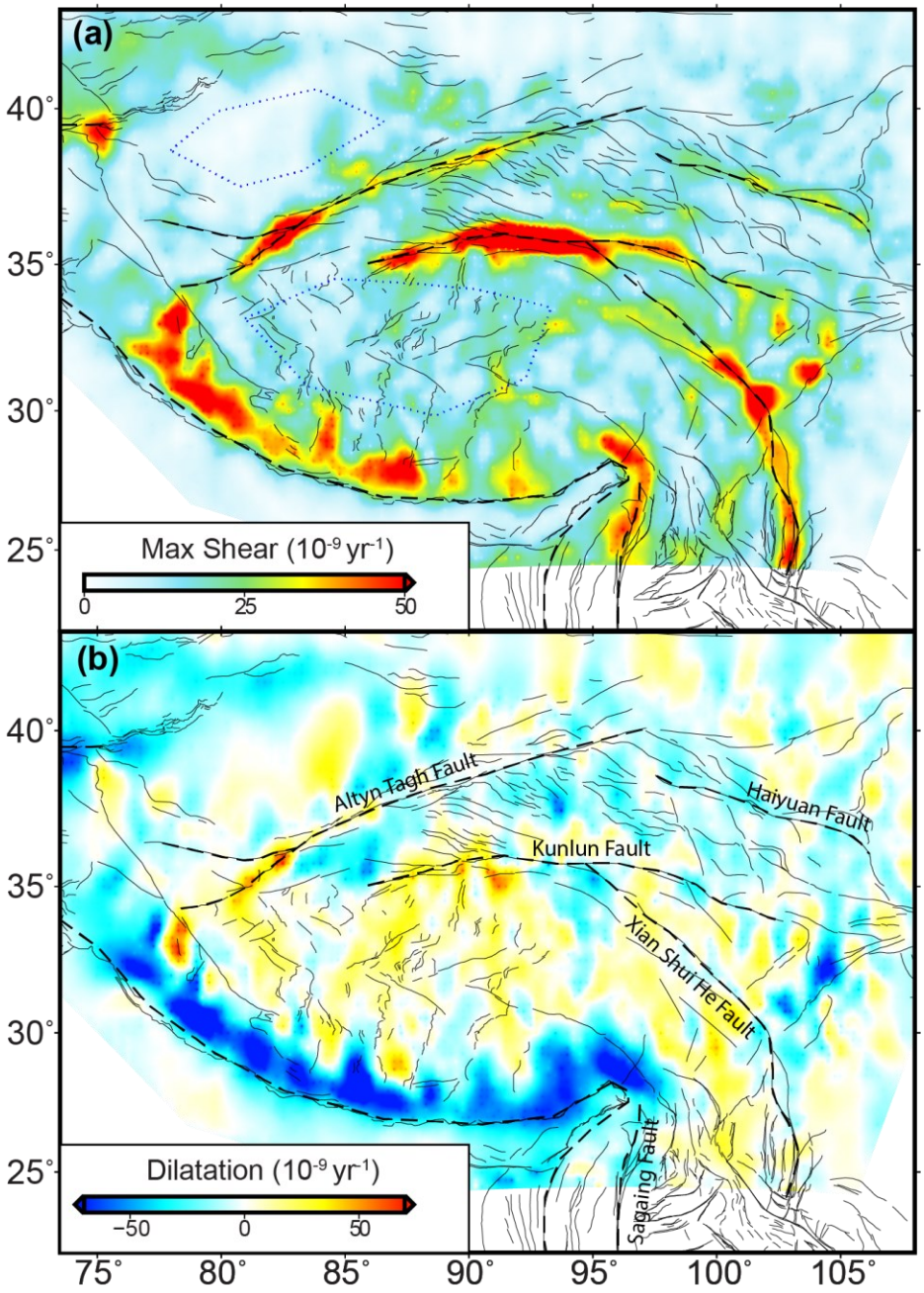

Figure 2: Components of the estimated horizontal strain rate field. (a) Maximum shear strain rate and (b) dilatation derived from the continuous smooth velocity field model (Fig. 3a, S2). Thick dashed black lines show the major faults we include in our geodynamic model (thin black lines are from the Global Earthquake Model (*40*). The dotted blue regions of the Tarim Basin and Tibetan Plateau in (a) are used for calculating strain statistics.

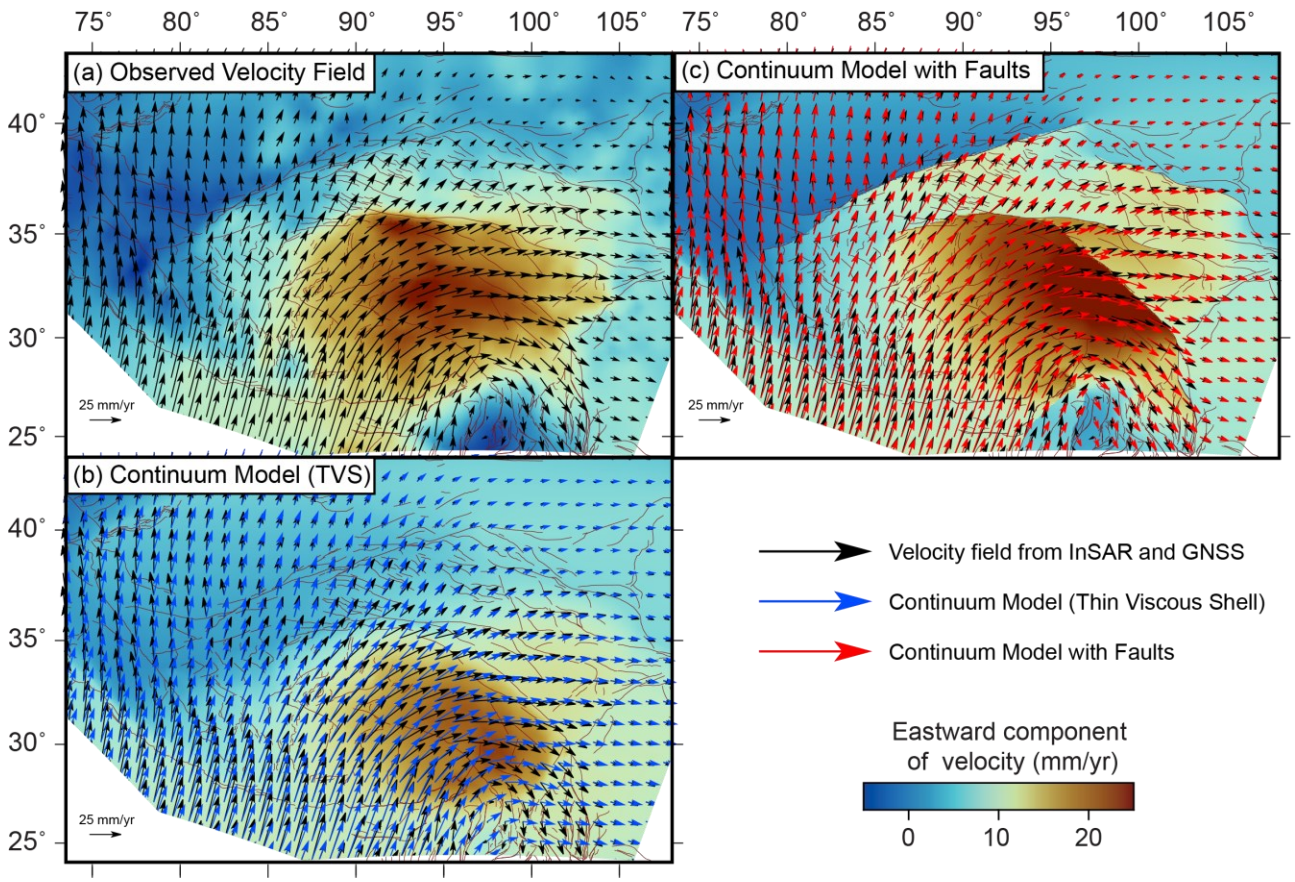

Figure 3: Comparison of observed and modelled velocity fields. (a) Velocity field derived from joint inversion of GNSS and InSAR; (b) velocities predicted by a thin viscous shell model with variable strength but no faults (rms misfit 4.9 mm/yr); (c) velocities predicted by faulted thin viscous shell model (rms misfit 3.5 mm/yr). In each case the vectors show velocities sampled on a 1-degree grid, and the colors show the east component of the velocity field. Dark red lines are faults from the Global Earthquake Model database. We do not expect agreement very close to major faults between the model, which represents long-term motions, and observations, which are short-term interseismic deformation, because the seismogenic upper crust is locked in the interseismic period (*34*).

References

1. D. P. McKenzie, R. L. Parker, The North Pacific: an example of tectonics on a sphere. *Nature* **216**, 1276-1280 (1967).
2. C. DeMets, R. G. Gordon, D. F. Argus, Geologically current plate motions. *Geophysical Journal International* **181**, 1-80 (2010).
3. B. Isacks, J. Oliver, L. R. Sykes, Seismology and the new global tectonics. *Journal of geophysical research* **73**, 5855-5899 (1968).
4. J. P. Avouac, P. Tapponnier, Kinematic model of active deformation in central Asia. *Geophysical Research Letters* **20**, 895-898 (1993).
5. R. McCaffrey, Crustal block rotations and plate coupling. *Plate Boundary Zones*, 101-122 (2002).
6. P. England, D. McKenzie, A thin viscous sheet model for continental deformation. *Geophysical Journal International* **70**, 295-321 (1982).
7. W. Thatcher, How the Continents Deform: The Evidence From Tectonic Geodesy. *Annual Review of Earth and Planetary Sciences* **37**, 237-262 (2009).
8. P. England, J. Jackson, Uncharted seismic risk. *Nature Geoscience* **4**, 348-349 (2011).
9. P. C. England, G. A. Houseman, The Mechanics of the Tibetan Plateau. *Philos T Roy Soc A* **326**, 301-320 (1988).
10. P. Tapponnier *et al.*, Geology - Oblique stepwise rise and growth of the Tibet plateau. *Science* **294**, 1671-1677 (2001).
11. C. Kreemer, G. Blewitt, E. C. Klein, A geodetic plate motion and global strain rate model. *Geochemistry, Geophysics, Geosystems* **15**, 3849-3889 (2014).
12. W. Wang, X. Qiao, K. Ding, Present-day kinematics in southeastern Tibet inferred from GPS measurements. *Journal of Geophysical Research: Solid Earth* **126**, e2020JB021305 (2021).
13. R. Styron, Contemporary Slip Rates of All Active Faults in the Indo-Asian Collision Zone *Earth and Space Science Open Archive*, 52 (2023).
14. S. Lechmann, S. Schmalholz, G. Hetényi, D. May, B. Kaus, Quantifying the impact of mechanical layering and underthrusting on the dynamics of the modern India-Asia collisional system with 3-D numerical models. *Journal of Geophysical Research: Solid Earth* **119**, 616-644 (2014).
15. S. H. Bischoff, L. M. Flesch, Normal faulting and viscous buckling in the Tibetan Plateau induced by a weak lower crust. *Nature Communications* **9**, 1-9 (2018).
16. M. Wang, Z.-K. Shen, Present-Day Crustal Deformation of Continental China Derived From GPS and Its Tectonic Implications. *Journal of Geophysical Research: Solid Earth* **125**, e2019JB018774 (2020).
17. E. Attema *et al.*, Sentinel-1 ESA's new European radar observatory. *EUSAR 2008*, (2008).
18. M. Lazecký *et al.*, LiCSAR: An automatic InSAR tool for measuring and monitoring tectonic and volcanic activity. *Remote Sensing* **12**, 2430 (2020).
19. Y. Morishita *et al.*, LiCSBAS: An Open-Source InSAR Time Series Analysis Package Integrated with the LiCSAR Automated Sentinel-1 InSAR Processor. *Remote Sensing* **12**, 424 (2020).
20. H. Wang, T. Wright, Satellite geodetic imaging reveals high strain away from major faults of Western Tibet. *Geophys. Res. Lett.* **39**, L07303 (2012).

21. J. R. Weiss *et al.*, High-Resolution Surface Velocities and Strain for Anatolia From Sentinel-1 InSAR and GNSS Data. *Geophysical Research Letters* **47**, e2020GL087376 (2020).
22. J. C. Savage, W. Gan, J. L. Svarc, Strain accumulation and rotation in the Eastern California Shear Zone. *Journal of Geophysical Research: Solid Earth* **106**, 21995-22007 (2001).
23. Q. Ou *et al.*, Large-Scale Interseismic Strain Mapping of the NE Tibetan Plateau From Sentinel-1 Interferometry. *Journal of Geophysical Research: Solid Earth* **127**, e2022JB024176 (2022).
24. H. Ansari, F. De Zan, A. Parizzi, Study of systematic bias in measuring surface deformation with SAR interferometry. *IEEE Transactions on Geoscience and Remote Sensing* **59**, 1285-1301 (2020).
25. G. Zheng *et al.*, Crustal deformation in the India-Eurasia collision zone from 25 years of GPS measurements. *Journal of Geophysical Research: Solid Earth* **122**, 9290-9312 (2017).
26. T. Ingleby, T. Wright, Omori-like decay of postseismic velocities following continental earthquakes. *Geophysical Research Letters* **44**, 3119-3130 (2017).
27. T. J. Wright, J. R. Elliott, H. Wang, I. Ryder, Earthquake cycle deformation and the Moho: Implications for the rheology of continental lithosphere. *Tectonophysics* **609**, 504-523 (2013).
28. E. Hussain *et al.*, Constant strain accumulation rate between major earthquakes on the North Anatolian Fault. *Nature Communications* **9**, 1392 (2018).
29. T. Yamasaki, T. J. Wright, G. A. Houseman, Weak ductile shear zone beneath a major strike-slip fault: Inferences from earthquake cycle model constrained by geodetic observations of the western North Anatolian Fault Zone. *Journal of Geophysical Research: Solid Earth* **119**, 3678-3699 (2014).
30. J. Elliott, R. Walters, T. Wright, The role of space-based observation in understanding and responding to active tectonics and earthquakes. *Nature Communications* **7**, 13844 (2016).
31. P. England, P. Molnar, Active deformation of Asia: From kinematics to dynamics. *Science* **278**, 647-650 (1997).
32. L. M. Flesch, A. J. Haines, W. E. Holt, Dynamics of the India-Eurasia collision zone. *Journal of Geophysical Research-Solid Earth* **106**, 16435-16460 (2001).
33. C. Amante, B. W. Eakins, in *NOAA technical memorandum NESDIS NGDC-24,* N. G. D. Center, Ed. (2009).
34. J. Fang *et al.*, The Dynamics of the India-Eurasia Collision: Faulted Viscous Continuum Models Constrained by High-Resolution Sentinel-1 InSAR and GNSS Velocities. *submitted to Journal of Geophysical Research: Solid Earth (available at EarthArXiv.org; https://doi.org/10.31223/X5TM1F)*, (2023).
35. R. Burgmann, G. Dresen, Rheology of the lower crust and upper mantle: Evidence from rock mechanics, geodesy, and field observations. *Annual Review of Earth and Planetary Sciences* **36**, 531-567 (2008).
36. R. H. Sibson, Continental fault structure and the shallow earthquake source. *Journal of the Geological Society* **140**, 741-767 (1983).
37. This is formulated using the second invariant of these tensor quantities, so that the deformation is independent of the reference frame

38. C. DeMets, S. Merkouriev, S. Jade, High-resolution reconstructions and GPS estimates of India–Eurasia and India–Somalia plate motions: 20 Ma to the present. *Geophysical Journal International* **220**, 1149-1171 (2020).
39. W.-J. Zheng *et al.*, Late Quaternary slip rate of the South Heli Shan Fault (northern Hexi Corridor, NW China) and its implications for northeastward growth of the Tibetan Plateau. *Tectonics* **32**, 271-293 (2013).
40. R. Styron, M. Pagani, The GEM global active faults database. *Earthquake Spectra* **36**, 160-180 (2020).

Acknowledgments:

COMET is the UK Natural Environment Research Council's Centre for the Observation and Modelling of Earthquakes, Volcanoes and Tectonics, a partnership between UK Universities and the British Geological Survey.

Funding:

We acknowledge the following funders of this research:

NERC LiCS grant Refs NE/K011006/1, NE/K010867/1 (BP, TJW, GAH, AJH)

COMET National Capability grants 2014/2019/2021 (TJW, GAH, AJH, JRE, BEP)

NERC Earthquakes without Frontiers grant Refs NE/J02001X/1, NE/J01978X/1 (BP, TJW)

Royal Society Fellowship grant Ref URF\R\21106 (JRE)

Royal Society grant RF\ERE\210143 (JRE)

China Scholarship Council-University of Leeds Scholarship Ref 202006270022 (JF)

National Natural Science Foundation of China Ref 42274001 (HW).

Author contributions:

Conceptualization: TJW, GAH, BP

Methodology: TJW, GAH, JF, YM, AJH, LE, ML, QO, JCR, HW

Investigation: TJW, GAH, JF, YM

Visualization: TJW, JF, JCR, QO, YM

Funding acquisition: TJW, BP, JRE, JF

Writing – original draft: TJW

Writing – review & editing: All

Competing interests: Authors declare that they have no competing interests.

Data and materials availability: All data are available in the supplementary materials or online repositories.

Supplementary Materials for

High-resolution geodetic strain rate field reveals dynamics of the India-Eurasia collision

Authors: T.J. Wright[1]*, G.A. Houseman[1], J. Fang[1], Y. Maghsoudi[1], A.J. Hooper[1], J.R. Elliott[1], L. Evans[2], M. Lazecky[1], Q. Ou[1], B.E. Parsons[3], J.C. Rollins[1,4], L. Shen[1], H. Wang[5]

Affiliations:
[1]COMET, School of Earth and Environment, University of Leeds; Leeds, UK
[2]School of Earth, Atmosphere & Environment, Monash University, Clayton, VIC, Australia
[3]COMET, Department of Earth Sciences, University of Oxford; Oxford, UK
[4] GNS Science, Lower Hutt, New Zealand
[5] Department of Surveying Engineering, Guangdong University of Technology, Guangzhou, China

*Corresponding author. Email: t.j.wright@leeds.ac.uk

This PDF file includes:

Materials and Methods

InSAR processing

We processed data from ~23,200 Sentinel-1 SAR acquisitions to create ~82,500 interferograms using the COMET-LiCSAR system (*1*). This system was built to automatically create Sentinel-1 interferograms from 250-km-wide Interferometric Wide Swath data acquired over the continents. We divide that land surface up into 82 ascending and 84 descending frames that are typically 250 km long, and process interferometric networks in short-baseline configurations, typically aiming to connect each epoch to the closest 4 epochs in time. In Tibet, most data is acquired with a 12 day revisit when there are two satellites operating in the Sentinel-1 constellation. We define some frames to be larger than the 250 km standard definition, typically where frame boundaries coincide with major faults, or where boundaries needed to be adjusted to coincide a switch from Sentinel-1A to -1B. All interferograms are available in Geotiff format via the COMET-LICSAR portal (https://comet.nerc.ac.uk/comet-lics-portal/) and via the CEDA archive (https://data.ceda.ac.uk/neodc/comet/data/licsar_products). Individual networks used for time series analysis in each frame can be viewed as part of the velocity field kmz data files (Available for reviewers in https://homepages.see.leeds.ac.uk/~eartjw/data/tibet/; on acceptance we will make these data fully available via the CEDA archive).

Estimating average line-of-sight velocities

We downsample the LiCSAR data from ~100 m to ~1 km resolution and calculate average line-of-sight velocities for each LiCSAR frame using the LiCSBAS code (*2*), which finds the best fit long-term velocity on a pixel-by-pixel basis, using the available short-baseline network. The approach accounts for any gaps in the network, and identifies and removes unwrapping errors found by checking closure phase around triangular loops. We additionally performed a careful visual inspection to remove all the remaining bad-quality interferograms prior to the LiCSBAS inversion. After the inversion, we masked noisy pixels using a number of noise indices, including the number of unclosed loops and the RMS of residuals in the small baseline inversion; we adjusted these parameters for each frame to optimize the results. We also removed a long-wavelength quadratic ramp from each LiCSAR frame, retaining only the feature of the velocity field that cannot be explained by long-wavelength ramps in the data. The line-of-sight velocities for all the frames used in this analysis can be downloaded from the CEDA archive (a kmz file showing the velocities is available for reviewers in https://homepages.see.leeds.ac.uk/~eartjw/data/tibet/; on acceptance we will make these data fully available via the CEDA archive).

Correcting for earthquakes

During the 2015-2021 observation period there were 7 earthquakes larger than Mw 5.5 in the area we processed (Table S1), of which 4 were larger than Mw 6 and only 1 was larger than Mw 7 (the 2021 Mw 7.3 Maduo Earthquake in Southern Qinghai, China). We made corrections to frames impacted by earthquakes larger than M_w 5.5 to ensure that the line-of-sight velocities are dominated by interseismic strain accumulation. We used four mitigation approaches:

a) For earthquakes occurring in 2015 we did not include any SAR acquisitions before the earthquake.
b) For earthquakes in 2021, we did not include any acquisitions after the earthquake

c) For some earthquakes, following the approach used by the Nevada Geodetic Laboratory for GNSS time series (*3*), we solved for and removed a coseismic offset in the LiCSBAS time series for all pixels within *s* km of the epicentre, where $s = 10^{(\frac{M}{2}-0.8)}$ km and *M* is the moment magnitude, before solving for the velocity on the adjusted time series.
d) For other earthquakes, we nullified pixels within *s* km of the epicentre in any interferogram spanning the earthquake and the first 2-3 months of postseismic data, before calculating the line-of-sight velocity with LiCSBAS.

For earthquakes in the period 2016-2020, methods (c) and (d) were both tried and the approach that gave the cleanest result visually was chosen. Table S1 lists the approach used for the final velocity field for each frame and earthquake.

GNSS compilation

Building on the work of Stevens and Avouac (*4*), we compiled GNSS data (and their uncertainties) throughout Asia from the Global Strain Rate Model 2.1 (*5*), from the updated MIDAS velocity set (*3; accessed 2021*), and from literature published since 2014 (*6-39*).This yields 10,290 horizontal (east and north), and 1,126 vertical velocities in the region (73.5 to 110 E and 24 to 43 N). We rotate these velocities into the Kreemer, Blewitt and Klein (*5*) definition of the fixed-Eurasia reference frame (assistance provided by Victoria Stevens, 2020), yielding the velocity field in Fig. S10. We then keep only the horizontal or vertical velocities that have estimated uncertainties of <=1.5 mm/yr, were derived from at least 2.5 years of data (following *3*) [Blewitt et al., 2018], and (if campaign data) were derived using at least 3 site occupations (following *40*). This leaves 8,608 horizontal velocities and 927 vertical velocities (Fig. S11). Finally, we then take the median of velocities at stations within 5 km of one another, including those at the same station published by different studies. This yields 1,569 east velocities, 1,569 north velocities, and 800 vertical velocities in the study region (Fig. S12). (Available for reviewers in https://homepages.see.leeds.ac.uk/~eartjw/data/tibet/; on acceptance we will make these data fully available via the CEDA archive).

Velocity Field Generation

To create a unified velocity field that fits the GNSS and InSAR data, we follow the procedure developed by (*41*). We first establish a triangular mesh covering the region of interest, using a set of nodes spaced by ~0.20 degrees in longitude and latitude (Fig. S1). We then use the *velmap* code to invert simultaneously for the best-fit 3D velocities at each node (Fig. S2), reference frame adjustment parameters for each InSAR frame, and a linear-with-height atmospheric correction term for each frame. The reference frame adjustment parameters consist of a second-order polynomial surface. Before inverting for the velocity field, InSAR data are downsampled to 5 km resolution. Because of the high level of noise in existing estimates of the vertical velocities, we only use the horizontal component of the GNSS velocities, setting the nominal vertical velocity for each GNSS observations to 0 ± 2 mm/yr, which allows for the inverted velocity field to have a vertical component if required by the InSAR data. Velocities at observation points (in the InSAR and GNSS) are linked to the velocities at the nodes of the mesh using linear interpolation functions, which account for variations in the satellite line of sight (*41*), and we minimize the weighted square misfit between the observations and predictions. To account for noise and data gaps, regularization is required to obtain a physically meaningful solution (*42*). We achieve this using Laplacian smoothing, adjusting the relative strength of the smoothing term to find a balance between solution roughness and misfit (Fig. S13). We use the spherical approximation

equations (A6 in *43*) to calculate, from the velocities on each vertex, horizontal strain rates and their uncertainties (Fig. S5).

As well as the velocities and strain rates, we can use the solution to create mosaics of ascending and descending line-of-sight velocities in a Eurasia reference frame, at the 1 km resolution, and including the linear-with-height atmospheric correction (Fig. S3). We can then invert pixel-by-pixel for the east-west (Fig. 1) and vertical velocities (Fig. S4) directly from the referenced line-of-sight velocities, without requirement for smoothing, using the north-south velocities from the smooth 3D velocity model as a constraint; InSAR has minimal sensitivity to the north-south velocities, but any error in the north-south velocity field will propagate into an error in the vertical velocities (*44*).

Data weighting and uncertainty estimation

We weight data sets using the formal uncertainties for the GNSS velocities as stated by their authors and the uncertainty in the line-of-sight velocities estimated (pixel-by-pixel) by LiCSBAS. Because we downsample InSAR data to 5 km before carrying out the velocity field inversion, and to make the inversion tractable, we do not include spatial covariances in the InSAR data in the velocity field inversion.

We exploit the fact that we have redundant and independent InSAR observations in many locations, due to overlapping tracks, to obtain an informal estimate of the uncertainties in the Eurasian-referenced InSAR and in the high-resolution (pixel by pixel) east-west and vertical velocities. For pixels where we have 4 independent observations of line-of-sight velocity (2 ascending tracks and 2 descending tracks), we can calculate 4 estimates of the east-west and vertical velocities (A1+D1; A1+D2; A2+D1; A2+D2), and make 2 sets of difference maps (A1+D1 vs A2+D2, A1+D2 vs A2+D1). These differences have standard deviations of 2.3 and 2.5 mm/yr in east-west and 2.0 and 1.8 mm/yr in vertical (Fig. S14). If the uncertainties are roughly equal between the independent estimates we can say that the uncertainty in east-west and vertical velocities for pixels where only two data sets exist are therefore ~1.7 and 1.3 mm/yr respectively.

For pixels where three line-of-sight data sets exist (i.e. 2 ascending + 1 descending; 1 ascending +2 descending), we can exclude one of the redundant data sets and calculate the standard deviation of the difference between the velocity of the excluded data set, Vel_r, and the line-of-sight velocity predicted for that excluded geometry from the eastward and vertical field generated with the remaining two data, Vel_p. These are 2.1 mm/yr when excluding data from an ascending track and 2.4 mm/yr when excluding data from a descending track. We can calculate the uncertainty on Vel_p as

$$\sigma_{Vel_p} = \sqrt{\left(los_e\ \sigma_{v_e}\right)^2 + \left(los_n\ \sigma_{v_n}\right)^2 + \left(los_u\ \sigma_{v_u}\right)^2}$$

where *los* and σ are the components of the unit vector and uncertainties for the east north and up components. We use the values estimated above of 1.7 and 1.3 mm/yr for σ_{v_e} and σ_{v_n} respectively, and use a conservative value of 3 mm/yr for σ_{v_n}, as north-south velocities are derived predominately from GNSS. From this information we can then estimate the average uncertainties on the original line-of-sight velocities, which are ~1.5 mm/yr for the ascending geometry and 1.9 mm/yr for the descending geometry. This compares well to the standard deviation of the residual between the InSAR data and the predicted velocities from velmap, which has a value of 1.7 mm/yr, and is a more realistic estimate than

the formal uncertainties from LiCSBAS, which are typically in the range 0.1 to 0.6 mm/yr (95% confidence).

Finally, we propagate uncertainties in the line-of-sight velocities to uncertainties in east-west and vertical velocities using the standard equations (*44*), to make maps of the uncertainty in the east and vertical velocities. The final spatial distribution of uncertainties are a function of the number of data sets and the viewing geometries at an individual pixel and range from 1.8 to 3 mm/yr and 1.6 to 2.4 mm/yr for the eastward and vertical uncertainties, respectively (95% confidence intervals) (Fig. S15).

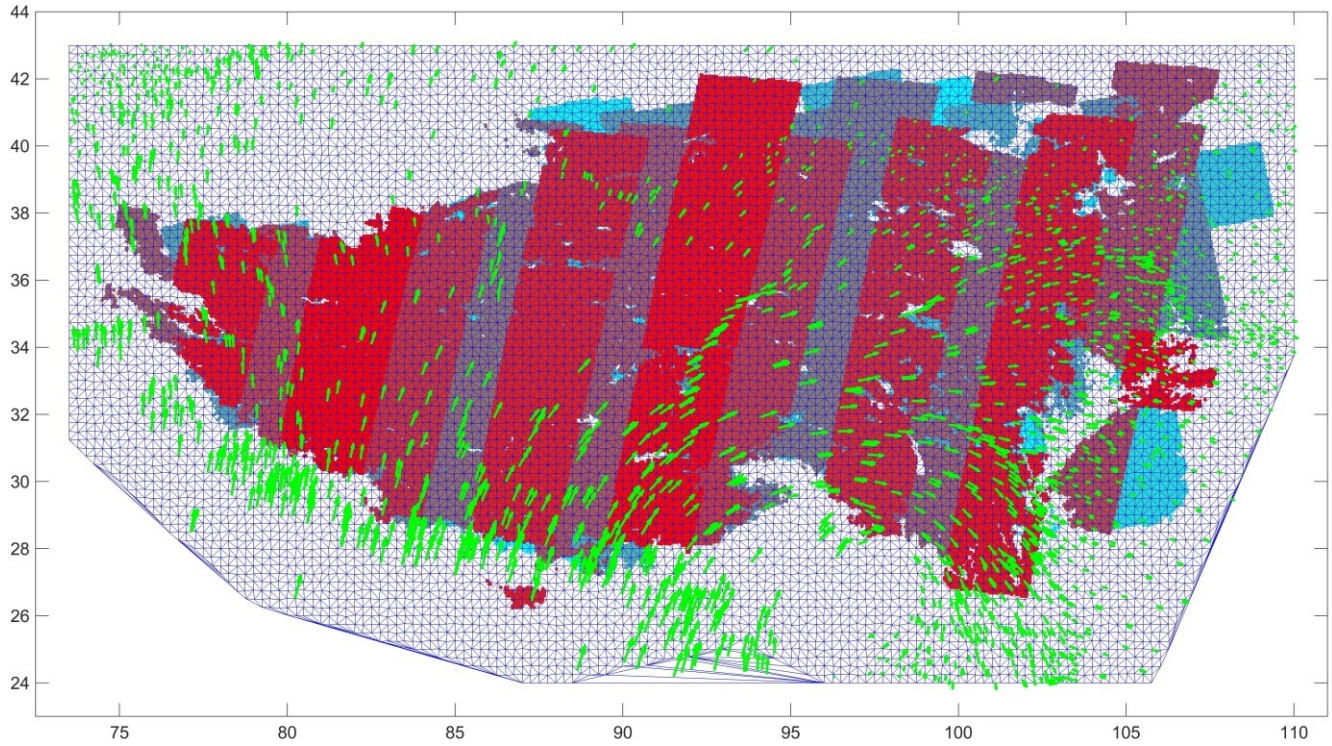

Fig. S1

Mesh and data used for the velocity field inversion. The blue lines show the element of the triangular mesh, with green arrows showing the GNSS data used (see Fig. S12). Colored dots show the location of coherent InSAR data used in the inversion. Different tracks are shown in different colors; colors have no other meaning.

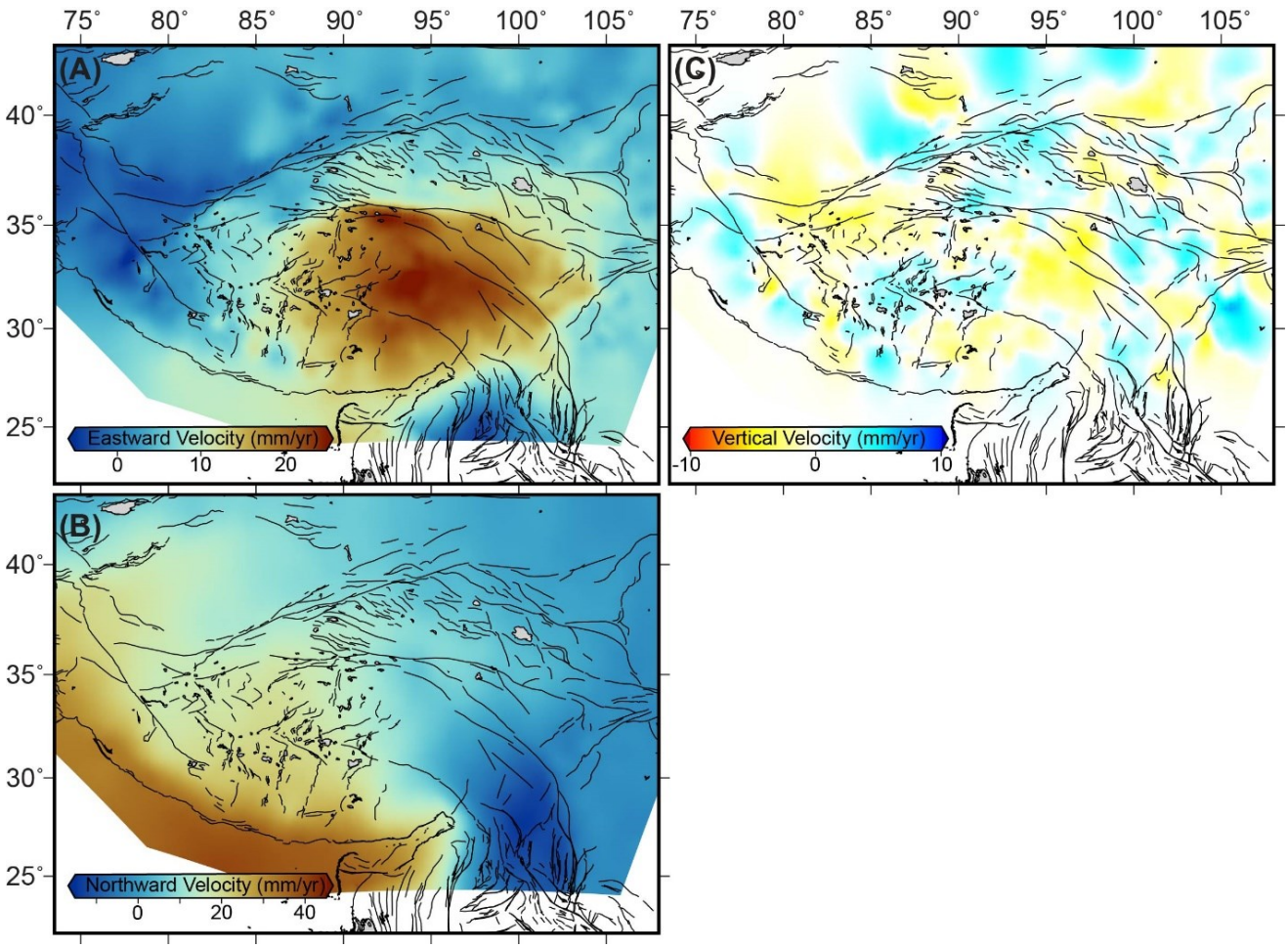

Fig. S2

Results of 3D velocity field inversion. (A) Eastward Velocity (positive values are towards east), (B) Northward Velocity (positive values are towards north), (C) Vertical Velocity (positive values are uplift). Black lines show active faults from the Global Earthquake Model (*45*).

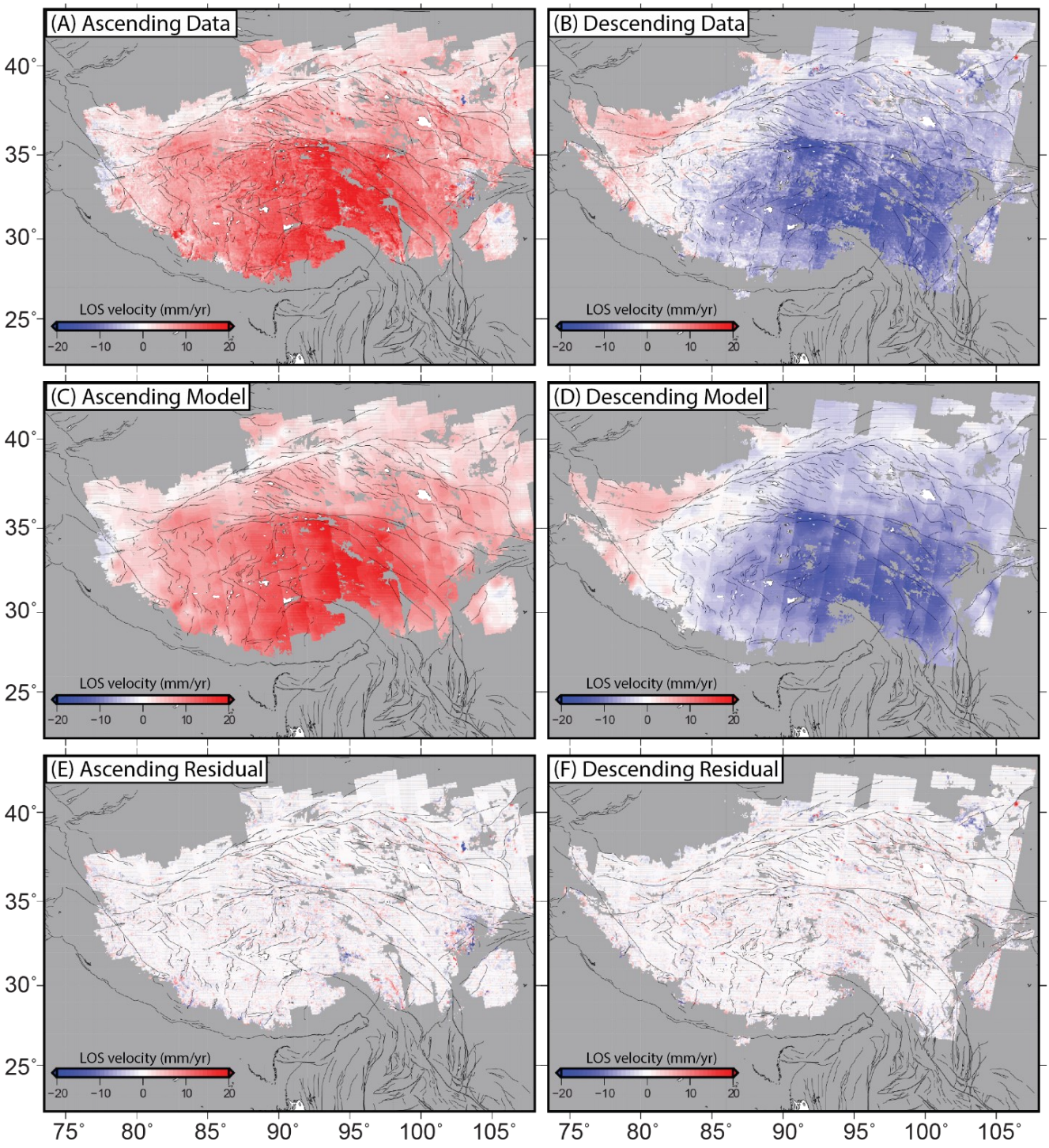

Fig. S3

Line-of-Sight (LOS) velocity mosaics for study area in a Eurasian Reference frame defined by GNSS. Red indicates motion away from the satellite. (A, B) show mosaics of observed LOS data in ascending and descending geometries respectively; (C, D) are the predicted LOS velocities from the inverted velocity field shown in Fig. S2; (E, F) show the residual LOS velocities that cannot be explained by the smooth inverted velocity field.

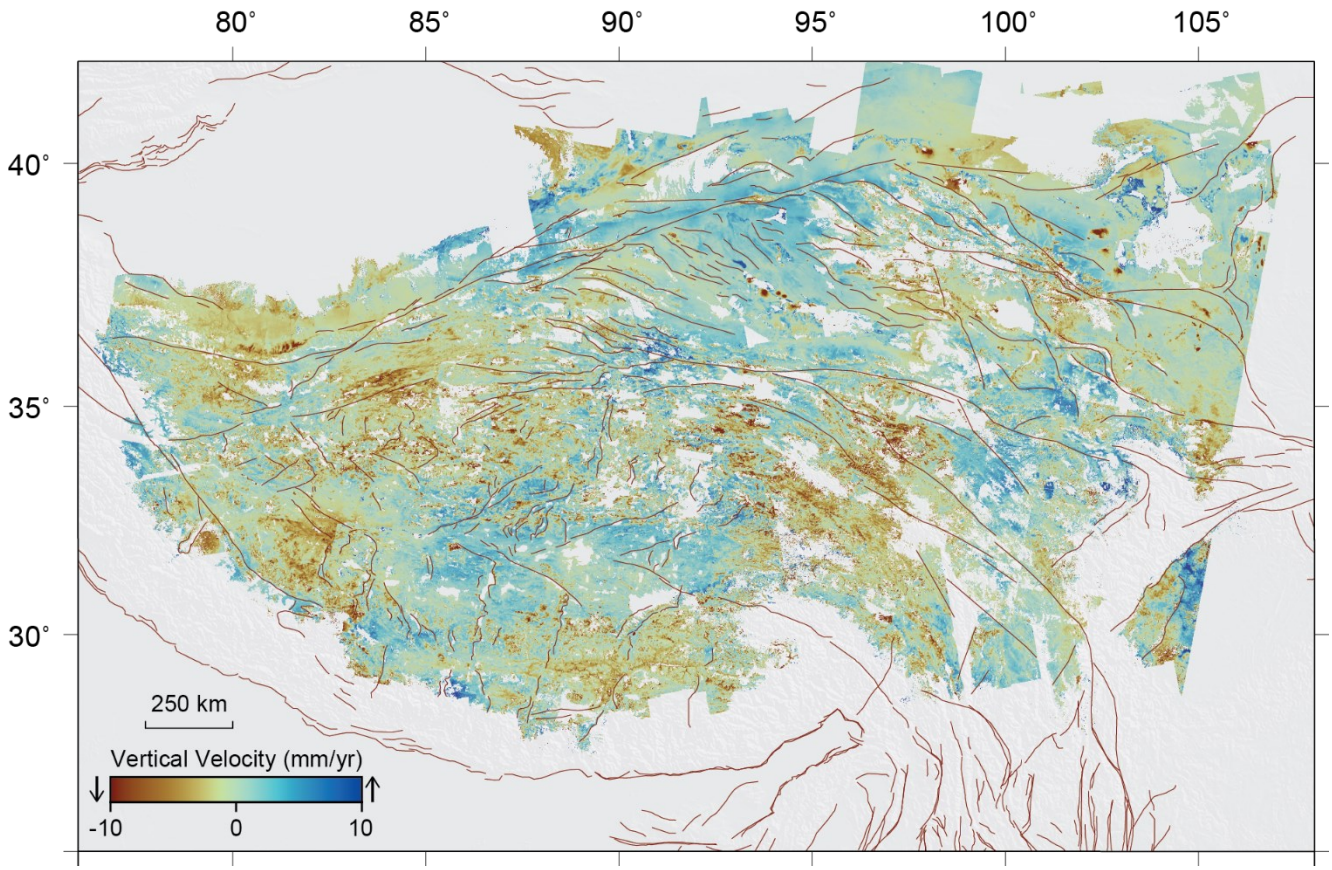

Fig. S4

Vertical velocity field for the Tibetan plateau at 1 km resolution, derived from combination of ascending and descending InSAR data shown in Fig. S3. Note that the LOS velocities are tied to GNSS in a Eurasian reference frame with the assumption that the average vertical velocity across the entire velocity field is 0.

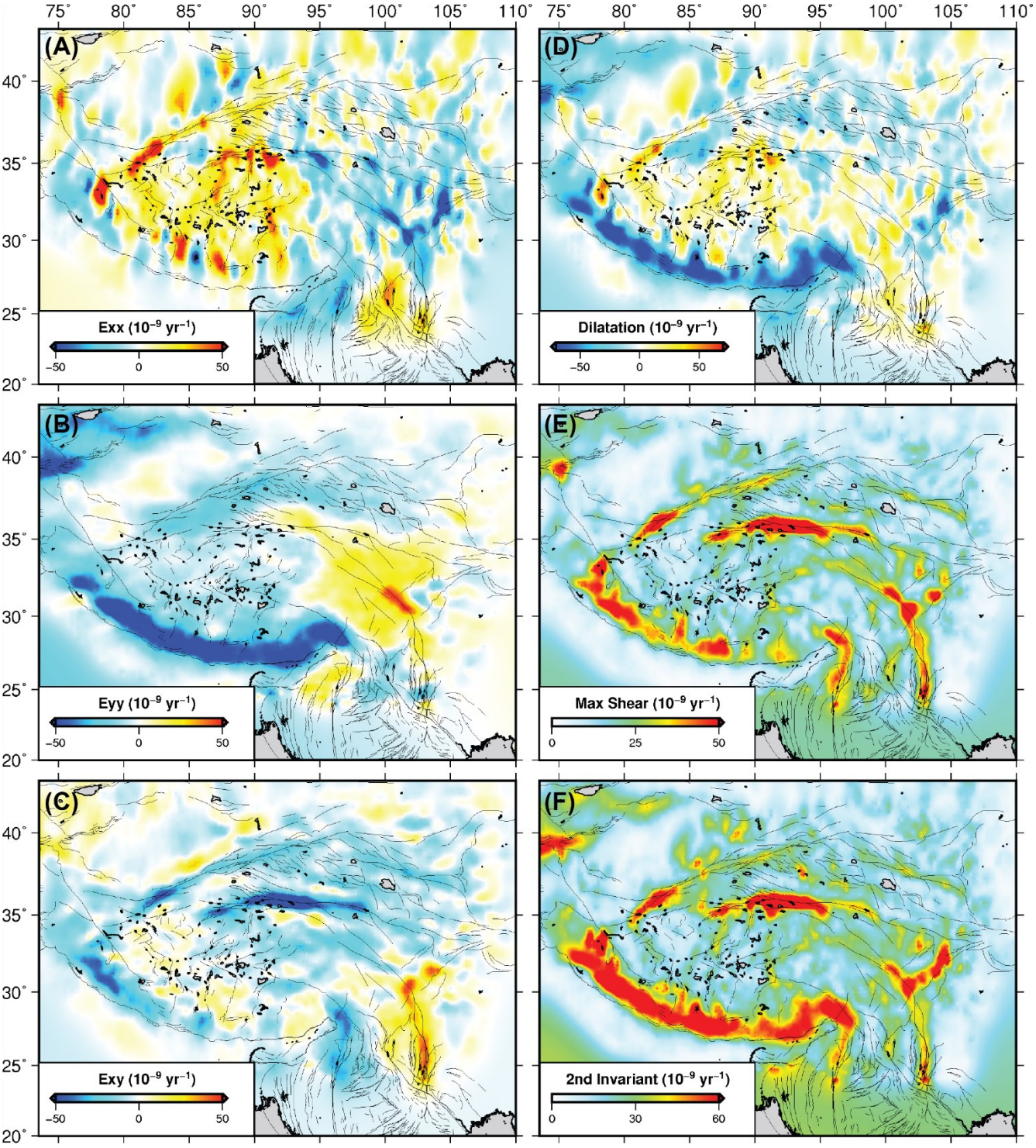

Fig. S5

Components of the horizontal strain rate tensor derived from the velocity field model shown in Fig. S2. Inset on each panel gives the component and color scale.

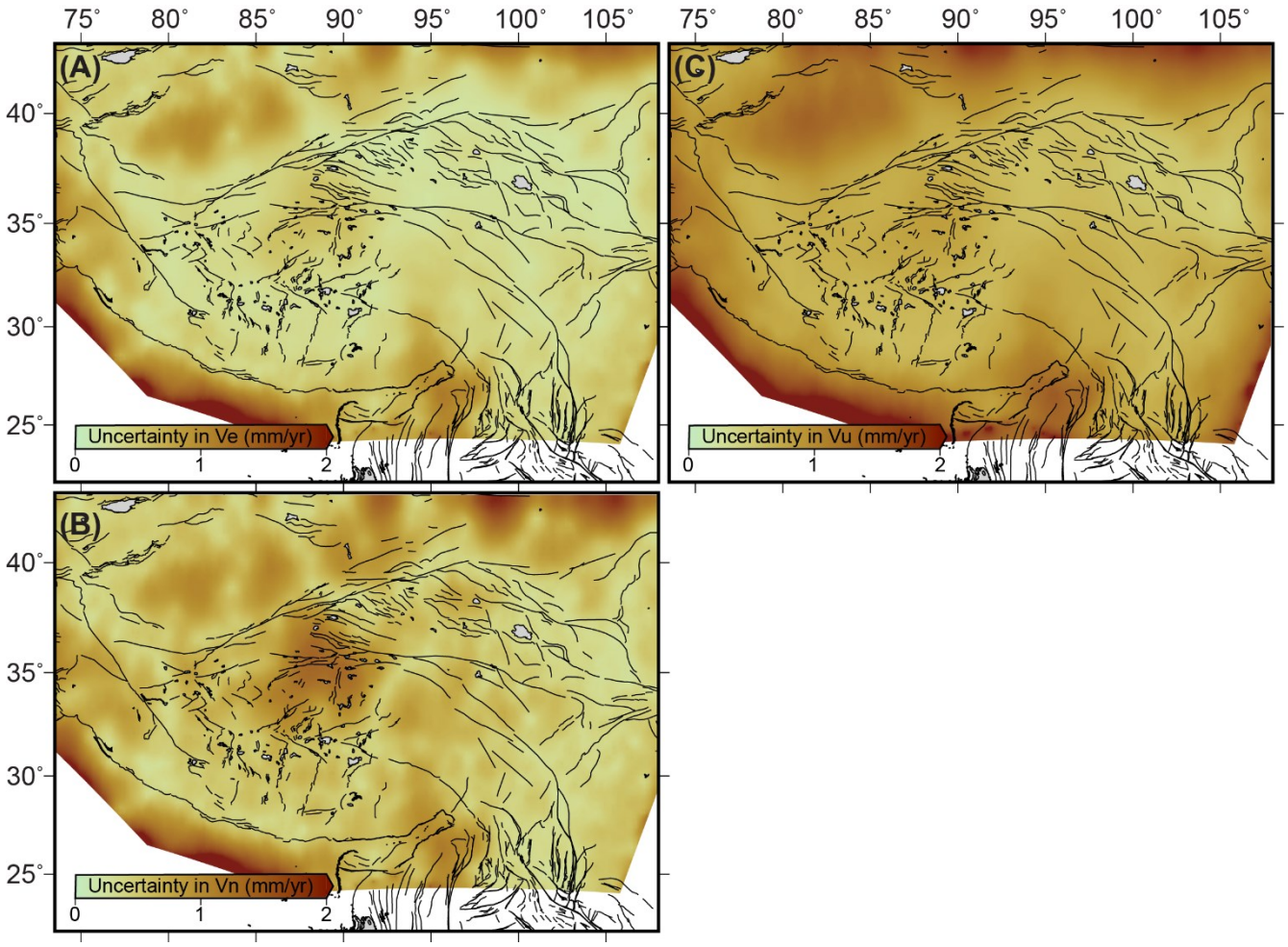

Fig. S6

Spatial distribution of uncertainties (1 standard deviation) of the (A) eastward, (B) northward, and (C) vertical velocity components of the velocity field shown in Fig. S2 estimated by the velocity field inversion.

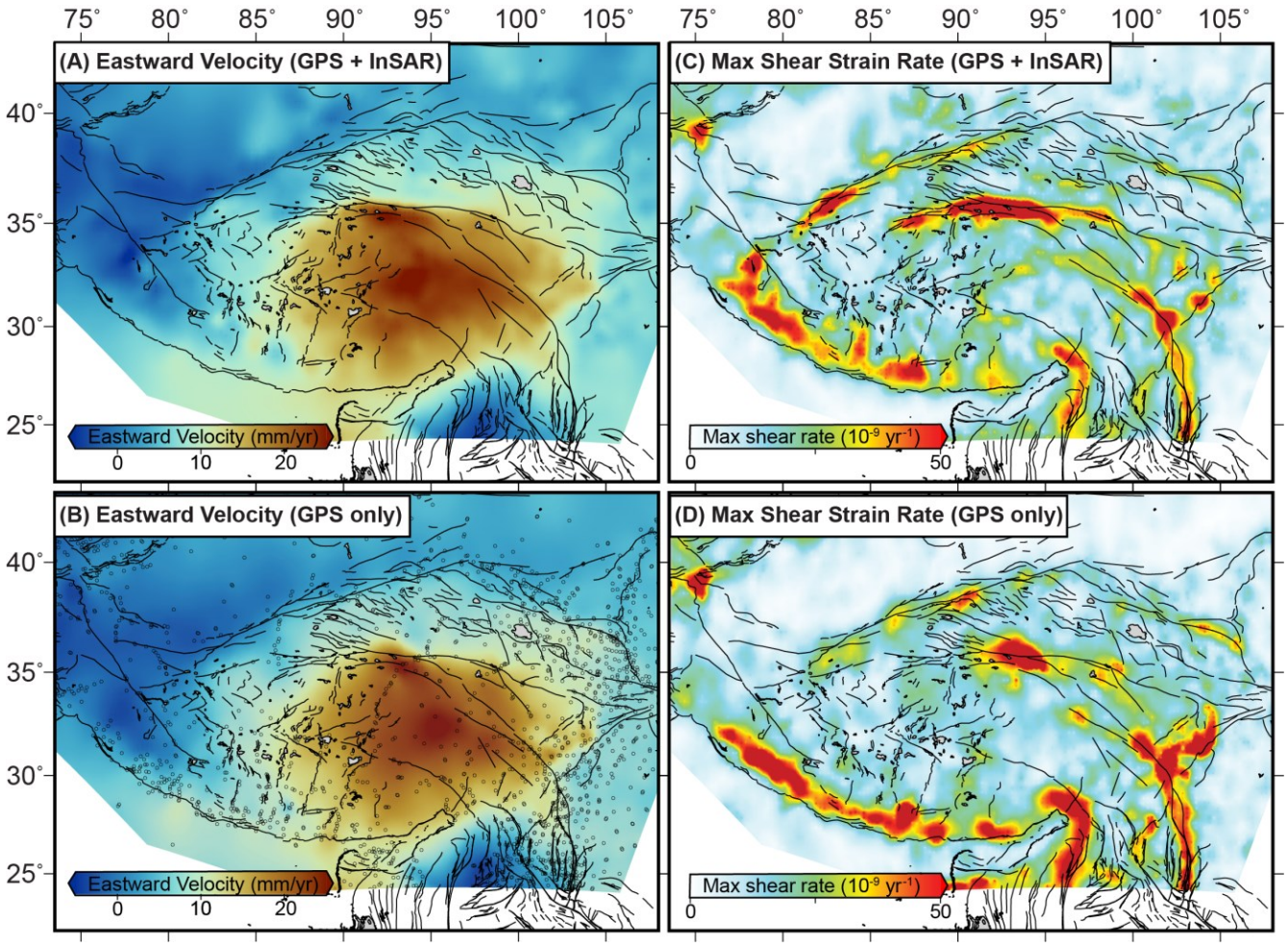

Fig. S7

Comparison of eastward velocities (A,B) and maximum shear strain rates (C,D) derived from the velocity field inversion using InSAR and GNSS (A,C) and GNSS data only (B,D). Inclusion of InSAR data adds extra detail to the velocity field, typically focusing more strain onto the major faults. Small circles in (B) show locations of GNSS sites and faults are from the Global Strain Rate Model.

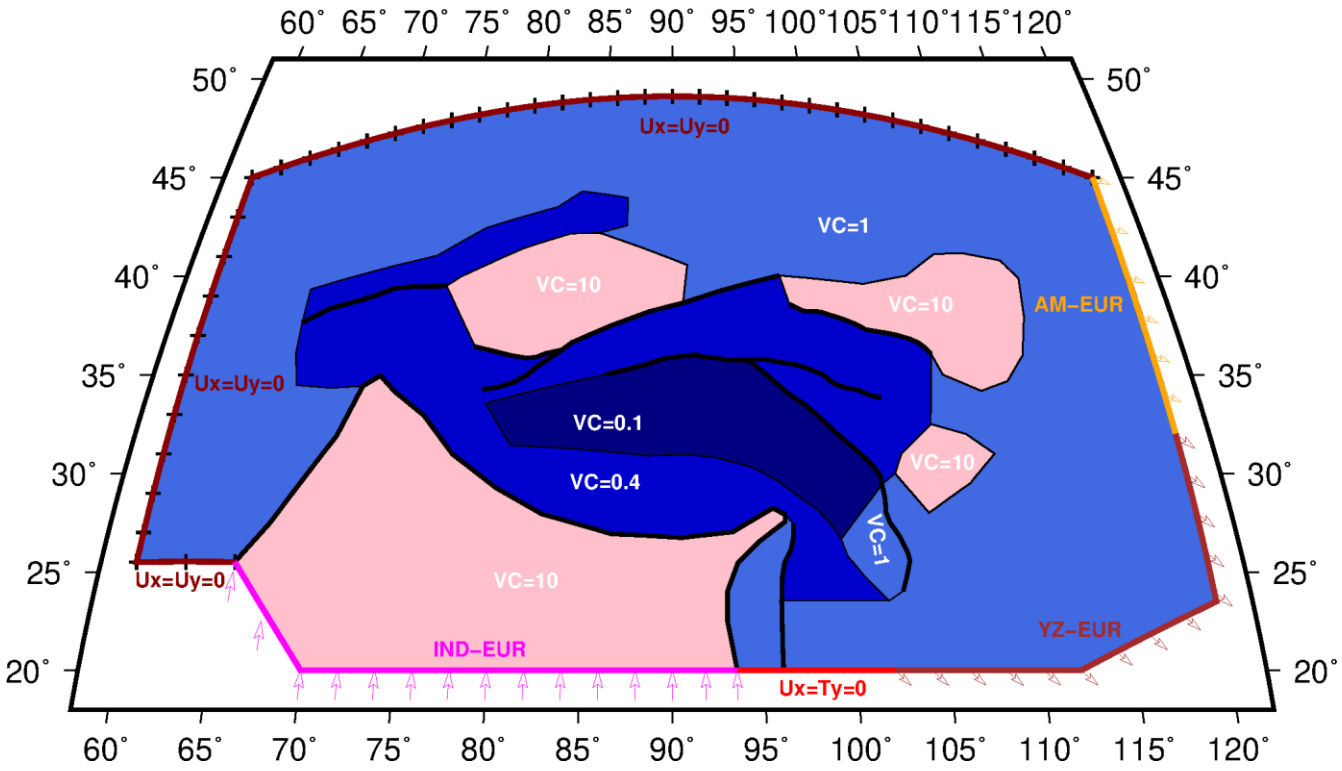

Fig. S8

Boundary and internal conditions for the dynamic faulted thin viscous shell model. The maroon outer boundary with black tick marks is held fixed with zero velocity, where the other boundaries are given velocities imposed by far-field plate motion poles of rotation, except for the small region east of India marked in red, where the eastward velocity and northward tractions are set to zero. Colors mark regions with different strengths, denoted by viscosity contrast coefficients (VC), relative normal Eurasia (VC=1); pink areas are strong, and dark blue areas are weaker than average. Thick black lines are the faults that are allowed to slip in this model.

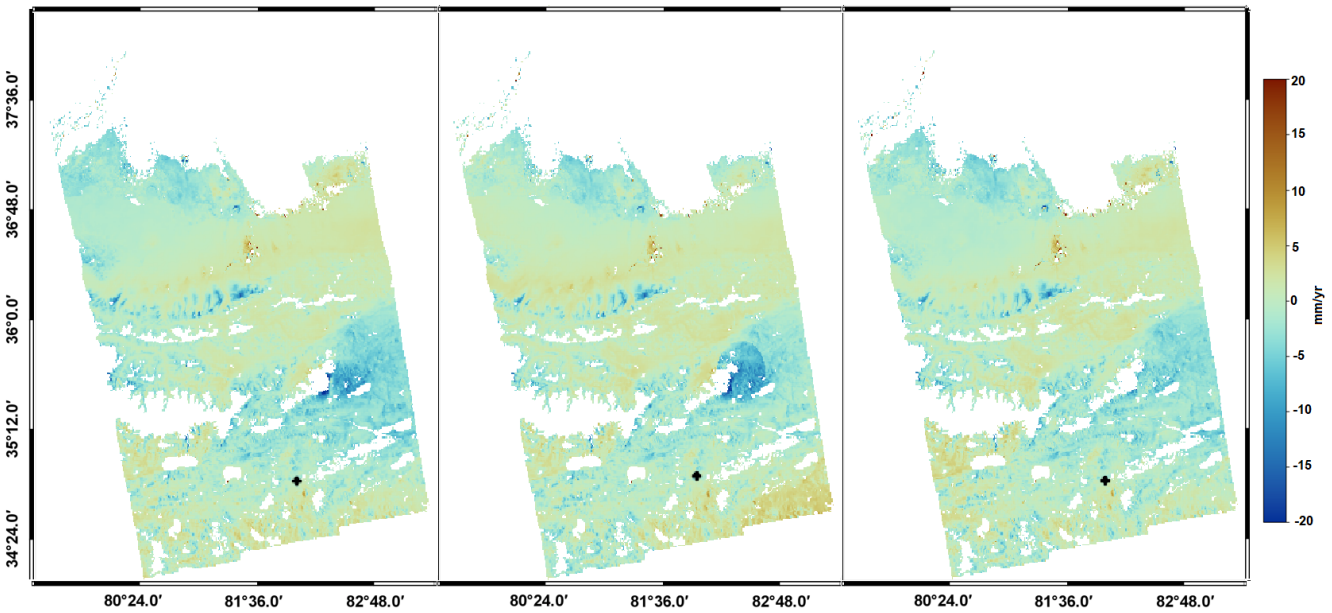

Fig. S9

Example of earthquake correction approach. The velocity map on the left is impacted by a Mw 6.3 earthquake, which occurred 278 km SE of Hotan, China, in June 2020 in the area marked by a dashed cirle. The central panel shows an attempt to remove the impact of the earthquake by nullifying pixels in any interferogram spanning the earthquake (method (d) in text). The panel on the right shows the result when we solve for a coseismic offset for the same pixels (method (c)), which is the preferred approach for this frame/event.

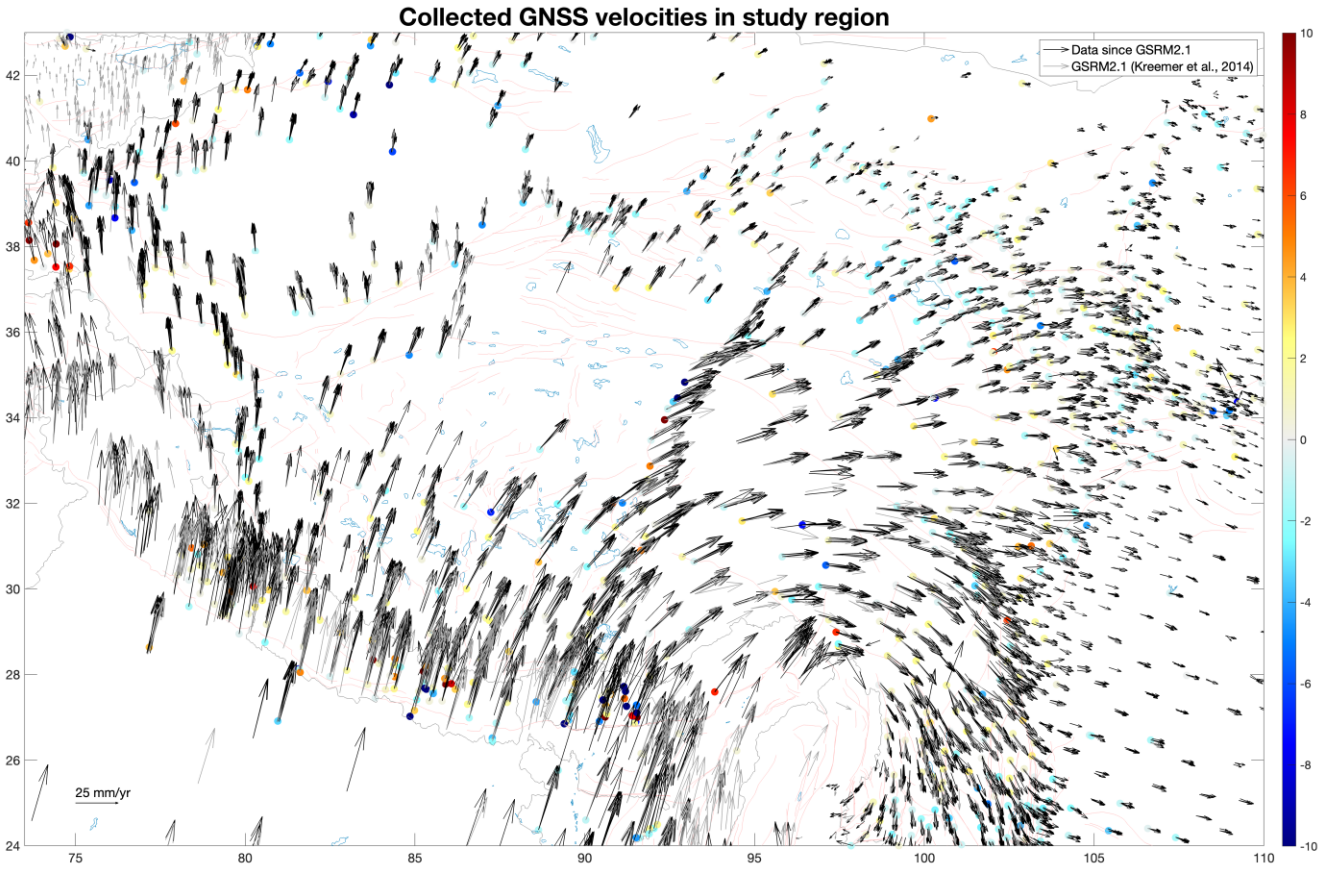

Fig. S10.
Compilation of GNSS velocities in the study region, rotated into the Eurasia reference frame defined by Kreemer, Blewitt and Klein (*5*). Vectors show horizontal motion, with bold lines indicating data that has been updated since Kreemer et al. Colors show vertical velocities with the scalebar in units of mm/yr (red is uplift).

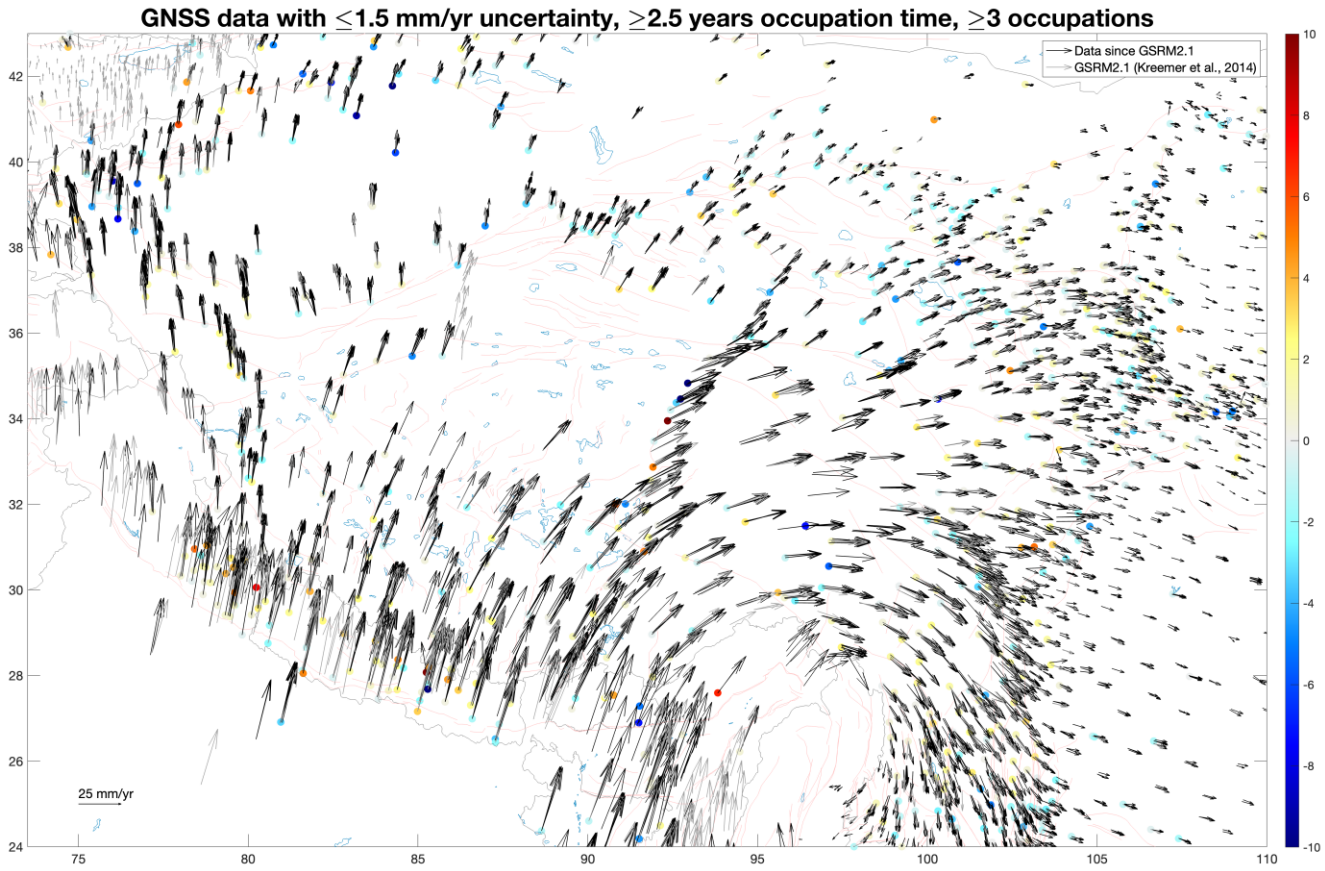

Fig. S11.

Same as Fig. S10. but excluding sites with uncertainties greater than or equal to 1.5 mm/yr, occupation times less than 2.5 years or fewer than 3 occupations.

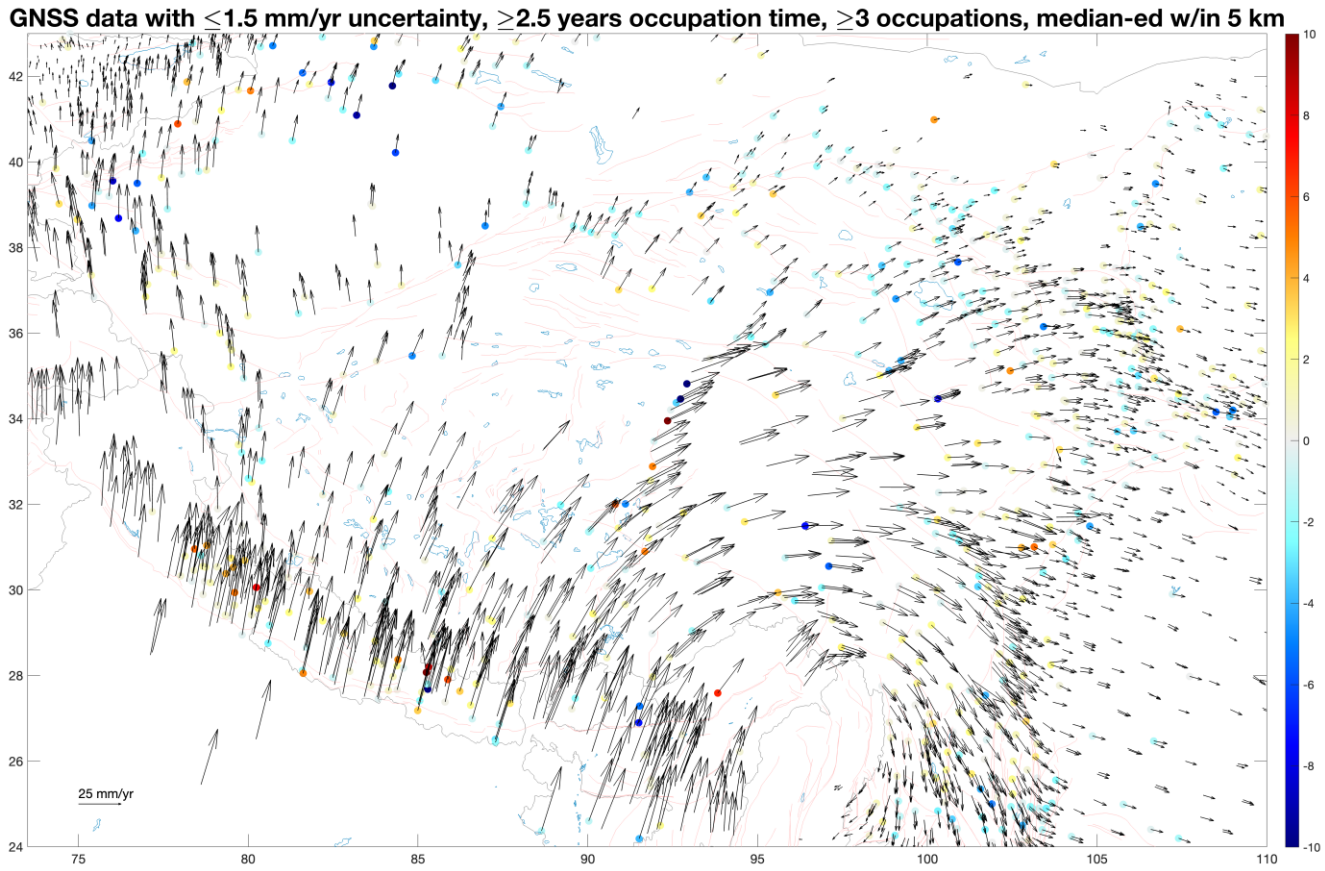

Fig. S12.

Same as Fig. S11 but only showing the median of velocities at stations within 5 km of one another (including those at the same station published by different studies). This is the velocity field we use in combination with InSAR data.

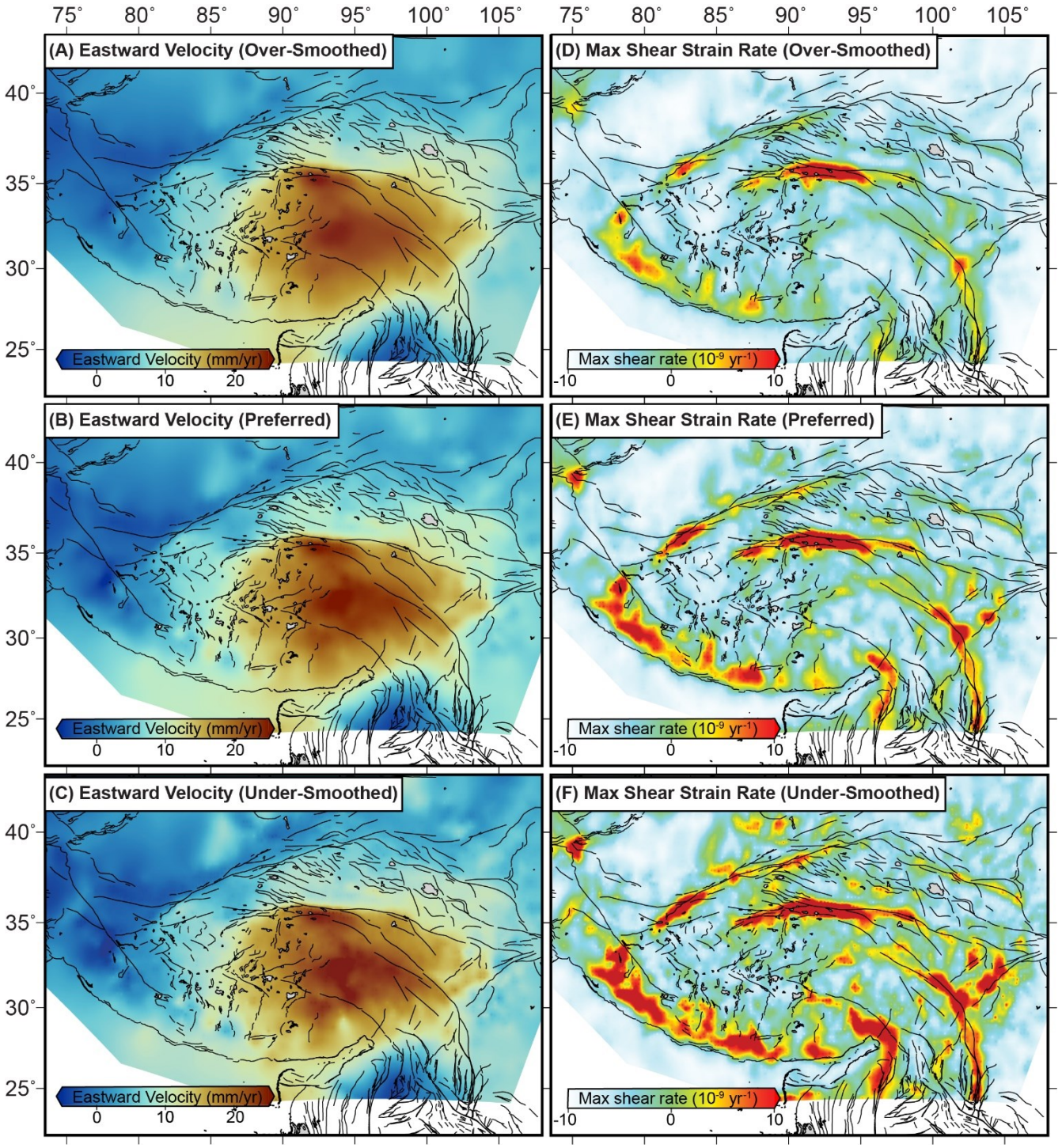

Fig. S13.

Three versions of the eastward velocity (A, B, C) and the maximum shear strain rate (D, E, F) from velocity field inversions with different smoothing factors. The top row (A, D) uses a smoothing factor of $10^{-0.4}$ and is over-smoothed; the bottom row (D, F) uses a smoothing factor of $10^{-1.2}$ and is under-smoothed. Our preferred model (B, E) uses a smoothing factor of $10^{-0.8}$.

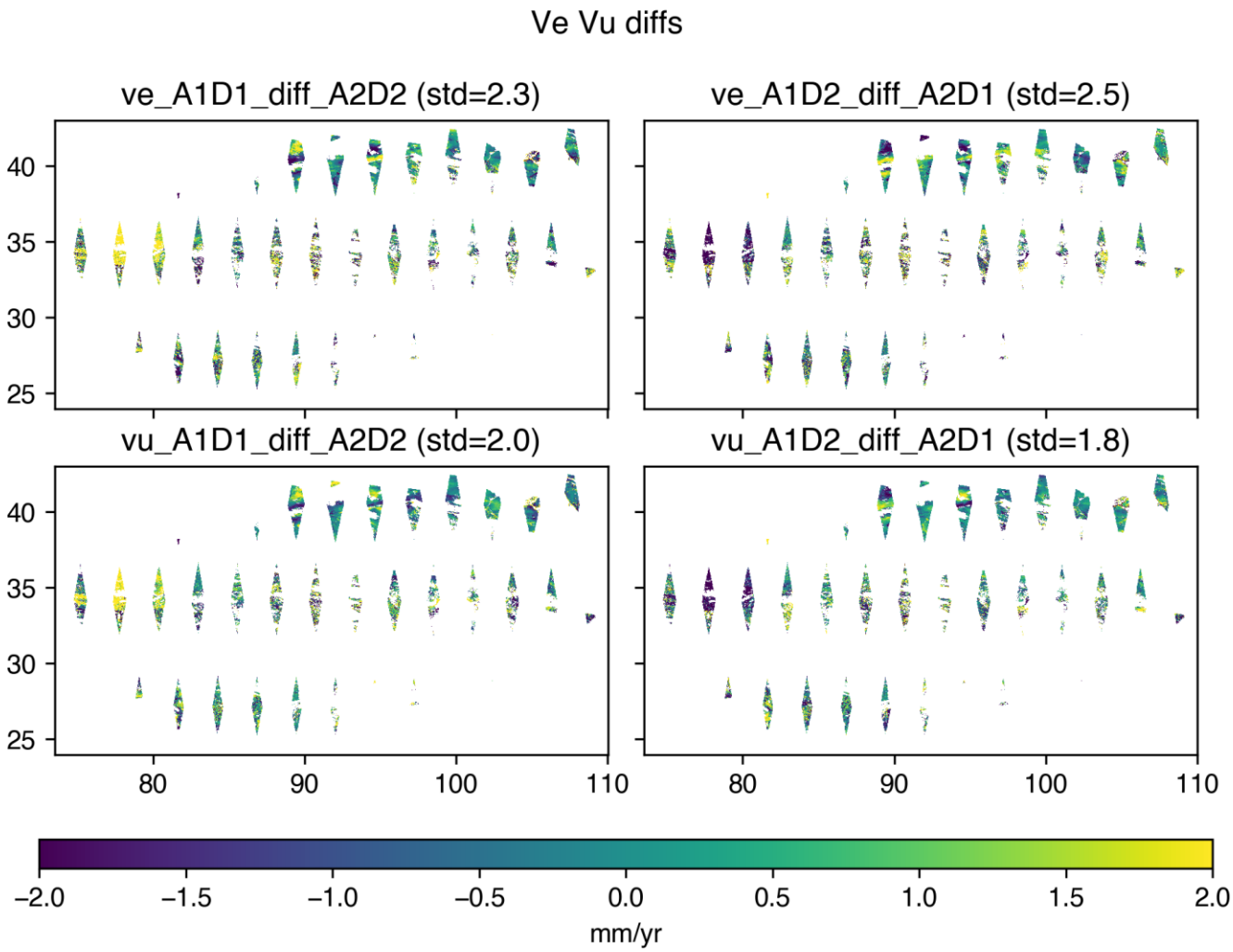

Fig. S14.
Difference maps between independent estimates of east-west and vertical velocities, for pixels where 4 independent observations (2 ascending and 2 descending) exist.

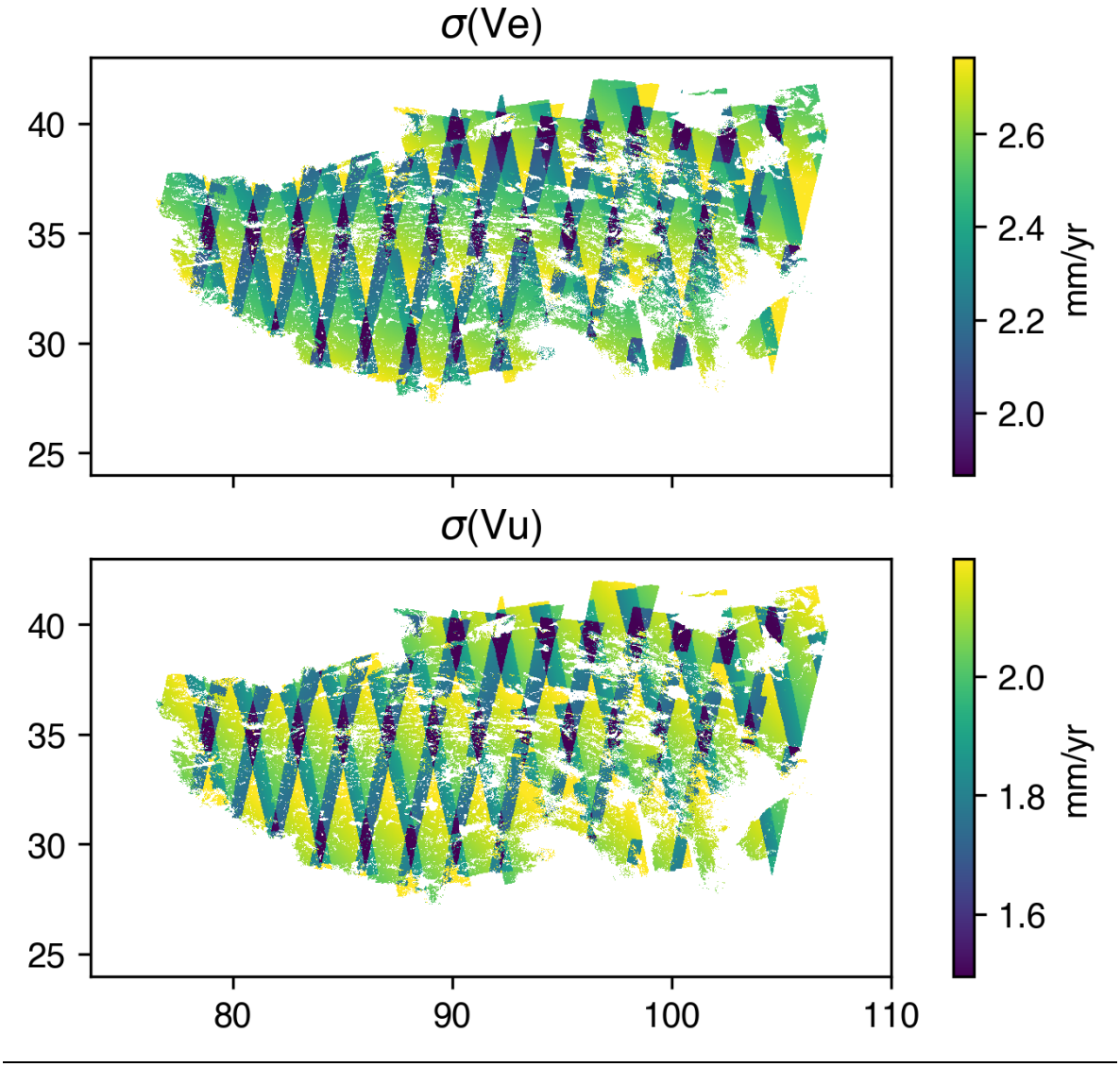

Fig. S15.
Estimates of uncertainty for 1 km grids of Ve and Vu.

Date	Lon	Lat	Magnitude and Location	Depth (km)	LiCSAR Frame	Approach
4/25/2015	87.317	28.390	M 5.7 - 69 km NE of Lobujya, Nepal	10.00	012A_06241_131313	a
4/25/2015	87.317	28.39	M 5.7 - 69 km NE of Lobujya, Nepal	10.00	121D_06067_131313	a
7/3/2015	78.154	37.459	M 6.4 - 57 km WNW of Zangguy, China	20.00	056A_05398_221919	a
7/3/2015	78.154	37.459	M 6.4 - 57 km WNW of Zangguy, China	20.00	129A_05337_131313	a
7/3/2015	78.154	37.459	M 6.4 - 57 km WNW of Zangguy, China	20.00	136D_05396_202020	a
12/23/2018	87.620	30.408	M 5.8 - 177 km NW of Rikaze, China	10.00	012A_06041_131313	c
12/23/2018	87.62	30.408	M 5.8 - 177 km NW of Rikaze, China	10.00	121D_05867_131313	c
3/20/2020	87.308	28.590	M 5.7 - 85 km NE of Lobujya, Nepal	10.00	012A_06241_131313	c
3/20/2020	87.308	28.59	M 5.7 - 85 km NE of Lobujya, Nepal	10.00	121D_06067_131313	c
6/25/2020	82.416	35.595	M 6.3 - 278 km SE of Hotan, China	10.00	085A_05378_202323	c
6/25/2020	82.416	35.595	M 6.3 - 278 km SE of Hotan, China	10.00	158A_05388_231919	c
6/25/2020	82.416	35.595	M 6.3 - 278 km SE of Hotan, China	10.00	165D_05381_242222	c
7/22/2020	86.864	33.144	M 6.3 - western Xizang	10.00	012A_05642_131313	c
7/22/2020	86.864	33.144	M 6.3 - western Xizang	10.00	121D_05668_131313	c
5/21/2021	98.251	34.598	M 7.3 - Southern Qinghai, China	10.00	099A_05615_131313	b
5/21/2021	98.251	34.598	M 7.3 - Southern Qinghai, China	10.00	106D_05447_131313	b
5/21/2021	98.251	34.598	M 7.3 - Southern Qinghai, China	10.00	106D_05646_131313	b

Table S1.

Details of earthquakes and corresponding LiCSAR frames where corrections for coseismic deformation were made, along with the approach used in each case. See supplementary methods text for description of the 4 approaches used.

1. M. Lazecký *et al.*, LiCSAR: An automatic InSAR tool for measuring and monitoring tectonic and volcanic activity. *Remote Sensing* **12**, 2430 (2020).
2. Y. Morishita *et al.*, LiCSBAS: An Open-Source InSAR Time Series Analysis Package Integrated with the LiCSAR Automated Sentinel-1 InSAR Processor. *Remote Sensing* **12**, 424 (2020).
3. G. Blewitt, W. C. Hammond, C. Kreemer, Harnessing the GPS data explosion for interdisciplinary science. *Eos* **99**, 485 (2018).
4. V. Stevens, J. Avouac, On the relationship between strain rate and seismicity in the India–Asia collision zone: implications for probabilistic seismic hazard. *Geophysical Journal International* **226**, 220-245 (2021).
5. C. Kreemer, G. Blewitt, E. C. Klein, A geodetic plate motion and global strain rate model. *Geochemistry, Geophysics, Geosystems* **15**, 3849-3889 (2014).
6. P. Barman, J. D. Ray, A. Kumar, J. Chowdhury, K. Mahanta, Estimation of present-day inter-seismic deformation in Kopili fault zone of north-east India using GPS measurements. *Geomatics, Natural Hazards Risk* **7**, 586-599 (2016).
7. H. Bisht *et al.*, GPS derived crustal velocity, tectonic deformation and strain in the Indian Himalayan arc. *Journal of Geodesy* **575**, 141-152 (2021).
8. M. Devachandra, B. Kundu, J. Catherine, A. Kumar, V. K. Gahalaut, Global positioning system (GPS) measurements of crustal deformation across the frontal eastern Himalayan syntaxis and seismic-hazard assessment. *Bulletin of the Seismological Society of America* **104**, 1518-1524 (2014).
9. F. Diao *et al.*, Slip rate variation along the Kunlun fault (Tibet): Results from new GPS observations and a viscoelastic earthquake-cycle deformation model. *Geophysical Research Letters* **46**, 2524-2533 (2019).
10. R. K. Dumka, B. S. Kotlia, G. C. Kothyari, J. Paikrey, S. Dimri, Detection of high and moderate crustal strain zones in Uttarakhand Himalaya, India. *Acta Geodaetica et Geophysica* **53**, 503-521 (2018).
11. R. K. Dumka, B. S. Kotlia, K. Kumar, G. S. Satyal, L. M. Joshi, Crustal deformation revealed by GPS in Kumaun Himalaya, India. *Journal of Mountain Science* **11**, 41-50 (2014).
12. V. K. Gahalaut, K. Gahalaut, R. K. Dumka, P. Chaudhury, R. K. Yadav, Geodetic evidence of high compression across seismically active Kachchh Paleorift, India. *Tectonics* **38**, 3097-3107 (2019).
13. P. K. Gautam *et al.*, Continuous GPS measurements of crustal deformation in Garhwal-Kumaun Himalaya. *Quaternary International* **462**, 124-129 (2017).
14. W. P. Ge, P. Molnar, Z. K. Shen, Q. Li, Present-day crustal thinning in the southern and northern Tibetan plateau revealed by GPS measurements. *Geophysical Research Letters* **42**, 5227-5235 (2015).
15. R. Guo, Y. Zheng, W. Tian, J. Xu, W. Zhang, Locking status and earthquake potential hazard along the middle-south Xianshuihe fault. *Remote Sensing* **10**, 2048 (2018).
16. T. D. Gupta *et al.*, Kinematics and strain rates of the Eastern Himalayan Syntaxis from new GPS campaigns in Northeast India. *Tectonophysics* **655**, 15-26 (2015).
17. S. Jade *et al.*, GPS-derived deformation rates in northwestern Himalaya and Ladakh. *International Journal of Earth Sciences* **100**, 1293-1301 (2011).
18. S. Jade *et al.*, Crustal deformation rates in Kashmir valley and adjoining regions from continuous GPS measurements from 2008 to 2019. *Scientific Reports* **10**, 1-11 (2020).

19. Y. Li *et al.*, Elastic block and strain modeling of GPS data around the Haiyuan-Liupanshan fault, northeastern Tibetan Plateau. *Journal of Asian Earth Sciences* **150**, 87-97 (2017).
20. R. Mallick *et al.*, Active convergence of the India-Burma-Sunda plates revealed by a new continuous GPS network. *Journal of Geophysical Research: Solid Earth* **124**, 3155-3171 (2019).
21. A. Marechal *et al.*, Evidence of interseismic coupling variations along the Bhutan Himalayan arc from new GPS data. *Geophysical Research Letters* **43**, 12,399-312,406 (2016).
22. S. Metzger *et al.*, Dense GNSS profiles across the northwestern tip of the India-Asia collision zone: Triggered slip and westward flow of the Peter the First Range, Pamir, into the Tajik Depression. *Tectonics* **39**, e2019TC005797 (2020).
23. Y. Pan *et al.*, Contemporary mountain-building of the Tianshan and its relevance to geodynamics constrained by integrating GPS and GRACE measurements. *Journal of Geophysical Research: Solid Earth* **124**, 12171-12188 (2019).
24. Y. Pan, W.-B. Shen, C. Shum, R. Chen, Spatially varying surface seasonal oscillations and 3-D crustal deformation of the Tibetan Plateau derived from GPS and GRACE data. *Earth and Planetary Science Letters* **502**, 12-22 (2018).
25. Y. Pan, W.-B. Shen, Contemporary crustal movement of southeastern Tibet: Constraints from dense GPS measurements. *Scientific Reports* **7**, 1-7 (2017).
26. Z. Pan, Z. Yun, Z. Shao, Contemporary crustal deformation of Northeast Tibet from geodetic investigations and a comparison between the seismic and geodetic moment release rates. *Physics of Earth Planetary Interiors* **304**, 106489 (2020).
27. M. Perry *et al.*, Little geodetic evidence for localized Indian subduction in the Pamir-Hindu Kush of Central Asia. *Geophysical Research Letters* **46**, 109-118 (2019).
28. X. Rui, D. S. Stamps, A geodetic strain rate and tectonic velocity model for China. *Geochemistry, Geophysics, Geosystems* **20**, 1280-1297 (2019).
29. Y. Sharma *et al.*, Spatial distribution of earthquake potential along the Himalayan arc. *Tectonophysics* **791**, 228556 (2020).
30. M. S. Steckler *et al.*, Locked and loading megathrust linked to active subduction beneath the Indo-Burman Ranges. *Nature Geoscience* **9**, 615-618 (2016).
31. X. Su *et al.*, Crustal deformation on the northeastern margin of the Tibetan plateau from continuous GPS observations. *Remote Sensing* **11**, 34 (2018).
32. R. K. Yadav *et al.*, Strong seismic coupling underneath Garhwal–Kumaun region, NW Himalaya, India. *Earth Planetary Science Letters* **506**, 8-14 (2019).
33. R. K. Yadav, V. K. Gahalaut, A. K. Bansal, Tectonic and non-tectonic crustal deformation in Kumaun Garhwal Himalaya. *Quaternary International* **585**, 171-182 (2021).
34. B. Zhao *et al.*, Crustal deformation on the Chinese mainland during 1998–2014 based on GPS data. *Geodesy and Geodynamics* **6**, 7-15 (2015).
35. B. Zhao *et al.*, Contemporary kinematics of the Ordos block, North China and its adjacent rift systems constrained by dense GPS observations. *Journal of Asian Earth Sciences* **135**, 257-267 (2017).
36. Y. Zhou *et al.*, Present-day crustal motion around the Pamir Plateau from GPS measurements. *Gondwana Research* **35**, 144-154 (2016).
37. G. Zheng *et al.*, Crustal deformation in the India-Eurasia collision zone from 25 years of GPS measurements. *Journal of Geophysical Research: Solid Earth* **122**, 9290-9312 (2017).
38. W. Wang, X. Qiao, S. Yang, D. Wang, Present-day velocity field and block kinematics of Tibetan Plateau from GPS measurements. *Geophysical Journal International* **208**, 1088-1102 (2017).

39. M. Wang, Z.-K. Shen, Present-Day Crustal Deformation of Continental China Derived From GPS and Its Tectonic Implications. *Journal of Geophysical Research: Solid Earth* **125**, e2019JB018774 (2020).
40. P. England, G. Houseman, J. M. Nocquet, Constraints from GPS measurements on the dynamics of deformation in Anatolia and the Aegean. *Journal of Geophysical Research: Solid Earth* **121**, 8888-8916 (2016).
41. H. Wang, T. Wright, Satellite geodetic imaging reveals high strain away from major faults of Western Tibet. *Geophys. Res. Lett.* **39**, L07303 (2012).
42. J. R. Weiss *et al.*, High-Resolution Surface Velocities and Strain for Anatolia From Sentinel-1 InSAR and GNSS Data. *Geophysical Research Letters* **47**, e2020GL087376 (2020).
43. J. Savage, W. Gan, J. Svarc, Strain accumulation and rotation in the Eastern California Shear Zone. *Journal of Geophysical Research: Solid Earth* **106**, 21995-22007 (2001).
44. T. Wright, B. Parsons, Z. Lu, Toward mapping surface deformation in three dimensions using InSAR. *Geophysical Research Letters* **31**, (2004).
45. R. Styron, M. Pagani, The GEM global active faults database. *Earthquake Spectra* **36**, 160-180 (2020).